Dynamic strain estimation for fatigue assessment of an offshore monopile wind turbine using filtering and modal expansion algorithms[☆,☆☆]

K. Maes[a,*], A. Iliopoulos[b,**], W. Weijtjens[c], C. Devriendt[c], G. Lombaert[a]

[a] *KU Leuven, Department of Civil Engineering, B-3001 Leuven, Belgium*
[b] *Vrije Universiteit Brussel, Mechanics of Materials and Constructions, B-1050 Brussels, Belgium*
[c] *Vrije Universiteit Brussel, Acoustics and Vibration Research Group, B-1050 Brussels, Belgium*

Abstract

Offshore wind turbines are exposed to continuous wind and wave excitation. The monitoring of high periodic strains at critical locations is important to assess the remaining lifetime of the structure. At some critical locations below the water level, direct measurements of the strains are not feasible. Response estimation techniques can then be used to estimate the strains from a limited set of response measurements and a system model. This paper compares a Kalman filtering algorithm, a joint input-state estimation algorithm, and a modal expansion algorithm, for the estimation of dynamic strains in the tower of an offshore monopile wind turbine. The algorithms make use of a model of the structure and a limited number of response measurements for the prediction of the strain responses. The strain signals obtained from the response estimation algorithms are compared to the actual measured strains in the tower.

Keywords: response estimation, Kalman filter, joint input-state estimation, modal expansion, system identification, offshore wind turbine

1. Introduction

Offshore wind turbines (OWTs) are exposed to continuous wind and wave excitation and loads originating from the rotor, a.k.a. rotor harmonics. These cyclic loads and their interaction with the turbine dynamics make fatigue life a design driver for offshore wind turbines. The continuous monitoring of the strain response time histories at fatigue hot spots, e.g. at the mud-line, is important to assess the remaining lifetime of the structure. For (offshore) wind turbines, two distinctive components in the strain response time history and consequently in the fatigue spectra can be identified. The low-frequent, near-static (< 0.5 Hz) strain cycles are related to variations in the

[☆] *Postprint submitted to Mechanical Systems and Signal Processing*
[☆☆] *Published version:* K. Maes, A. Iliopoulos, W. Weijtjens, C. Devriendt, and G. Lombaert. Dynamic strain estimation for fatigue assessment of an offshore monopile wind turbine using filtering and modal expansion algorithms. *Mechanical Systems and Signal Processing*, 76–77:592–611, 2016.

[*] Corresponding author. Tel.: +32 (0) 16 32 25 73
[**] Corresponding author. Tel.: +32 (0) 2 629 29 55
Email addresses: kristof.maes@bwk.kuleuven.be (K. Maes), alexandros.iliopoulos@vub.ac.be (A. Iliopoulos)

thrust loading of the turbine, e.g. due to gusts. This component can be estimated using the 1 Hz turbine SCADA-data [1] and thus in theory requires no direct strain measurements. The second component is linked to the turbine's dynamics and modal behavior. The corresponding dynamic strains are associated to a higher frequency-range (> 0.1 Hz) and contain additional sources of vibrations, such as turbulence, rotor harmonics, and wave-loading. These strain components are currently best determined using direct measurements of the strain. For some critical locations such a direct measurement is not feasible. For example, direct measurements of the strains at the mud-line require sensors installed prior to the pile-driving of the monopile foundation. As a consequence, the sensors cannot be installed on existing OWTs. Experience in the field has also shown that strain sensors are harder to maintain, are less reliable than accelerometers over long periods in time, and are more susceptible to installation errors.

When direct measurements of the strains are impossible, fatigue monitoring of a wind turbine over its lifetime can be performed (a) through estimation of the dynamic loads applied to the structure (force identification), or (b) through model-based extrapolation of a limited set of available response measurements (response estimation). Many algorithms for force identification have been proposed in the literature [2, 3, 4, 5]. A time-domain deconvolution approach was applied in [6] for the estimation of wind loads on a 50 m tall mast. Recently, various Kalman filter-based force identification techniques have been proposed [7, 8, 9, 10, 11]. These techniques allow for online reconstruction of the dynamic loads applied to a structure. Hwang et al. proposed the identification of wind loads in the modal space, through the combined use of the Kalman filter and recursive least-squares estimation [12]. The approach was verified using wind tunnel experiments in [13]. A slightly modified version of the algorithm proposed in [12] was used by Niu et al. in [14] to reconstruct the wind loads on the Canton tower. Klinkov and Fritzen [15] adopted a robust observer technique for estimating the wind loads on a 5 MW wind turbine. This technique applies to both linear and nonlinear systems.

Response estimation techniques can be used to estimate the strains from a limited set of response measurements (accelerations, strains, etc.) and a system model. Various approaches for the estimation of stresses and strains using response estimation techniques are presented in the literature. Hjelm et al. [16] presented a strain estimation technique often referred to as modal expansion or full-field strain prediction [17]. This technique was further explored in [18] and was validated for predicting accelerations on an OWT in [19]. Other approaches make use of time varying auto-regressive models [20] and Kalman state estimation. The latter approach was introduced in the field of structural dynamics by Papadimitriou et al. in [21], where acceleration measurements are used as input to the Kalman filter to obtain the strain at unmeasured locations. Smyth and Wu [22] used the Kalman filter for the fusion of displacement and acceleration data obtained at different sampling rates. The displacement signals obtained after fusion are found to be more accurate than the original displacement data. The Kalman filter based response estimation was investigated numerically and experimentally in [23], for the special case of excitation characterized by low frequency variations. The paper also explores the advantages of data fusion, i.e. the simultaneous integration of multiple types of measurements, for example acceleration and strain measurements. It was numerically verified by Jo and Spencer [24] that the combination of acceleration and strain data in conjunction with the Kalman filter results in better estimates compared to the ones obtained from the sole use of acceleration or strain data.

In cases where state estimation is performed for nonlinear or uncertain dynamic systems, e.g. systems with time varying characteristics, the standard Kalman filter can no longer be applied for

state estimation. Several extensions of the Kalman filter for nonlinear dynamic systems have been proposed. One well known application in the literature is the simultaneous estimation of the system states and unknown system parameters, which is referred to as joint state and parameter estimation. Some common used algorithms for joint state and parameter estimation are the unscented Kalman filter (UKF) [25, 26], the extended Kalman filter (EKF) [27], and the particle filter [25, 28]. A comprehensive overview of the current state of the art can be found in [29]. The extensions of the Kalman filter for nonlinear systems are not further considered in this paper.

Verification of dynamic strain estimation using filtering techniques so far is mostly based on numerical simulations, where measurement errors are introduced by adding white noise to the simulated response signals, or on laboratory experiments. This paper presents a full-scale verification of two filtering algorithms and a modal expansion algorithm, using data obtained from in situ measurements on an offshore monopile wind turbine in the Belgian North Sea [30]. The first algorithm is a Kalman filtering algorithm. The second algorithm is a joint input-state estimation algorithm that was originally proposed by Gillijns and de Moor in [31], introduced for response estimation in structural dynamics by Lourens et al. in [32], and applied to a (simulated) offshore wind turbine structure in [33]. The algorithm is further extended in [34] for application in presence of unknown stochastic excitation when accelerations are measured. The third algorithm is a state of the art modal expansion algorithm [16, 18, 19]. The response estimation algorithms make use of a model of the structure and a limited number of response measurements for the prediction of the dynamic strain in the tower of the turbine. The system model used in the strain estimation is constructed based on the mode shapes and natural frequencies obtained from a finite element model of the structure and the damping characteristics that are obtained from a prior operational modal analysis (OMA). The data used in the response estimation consists of accelerations and strains. The focus of the paper is on dynamic strain estimation. The estimation of low-frequent, near-static strain components is not considered.

The outline of the paper is as follows. In Section 2, the two filtering algorithms and the modal expansion algorithm, as well as their application for response estimation are briefly recapitulated. Next, Section 3 shows the verification of the proposed response estimation techniques using data obtained from a monitoring campaign on a monopile offshore wind turbine. Section 4 defines the future work that directly results from the work presented in this paper. Finally, in Section 5, the work is concluded.

2. Mathematical formulation

2.1. System model

Consider the following continuous-time equations governing the motion of a linear system discretized in space:

$$\mathbf{M}\ddot{\mathbf{u}}(t) + \mathbf{C}\dot{\mathbf{u}}(t) + \mathbf{K}\mathbf{u}(t) = \mathbf{S}_{\mathrm{p}}(t)\mathbf{p}(t) \tag{1}$$

where $\mathbf{u}(t) \in \mathbb{R}^{n_{\mathrm{dof}}}$ is the vector of displacements (translations and/or rotations), and $\mathbf{M}$, $\mathbf{C}$, and $\mathbf{K} \in \mathbb{R}^{n_{\mathrm{dof}} \times n_{\mathrm{dof}}}$ are the mass, damping, and stiffness matrix of the system, respectively, with n_{dof} the number of degrees of freedom in the system model. The excitation force is written as the product of a selection matrix $\mathbf{S}_{\mathrm{p}}(t) \in \mathbb{R}^{n_{\mathrm{dof}} \times n_{\mathrm{p}}}$, specifying the force locations, and a time history vector $\mathbf{p}(t) \in \mathbb{R}^{n_{\mathrm{p}}}$, with n_{p} the number of forces.

The undamped eigenvalue problem corresponding to Eq. (1) reads:

$$\mathbf{K}\boldsymbol{\phi}_j = \omega_j^2 \mathbf{M}\boldsymbol{\phi}_j \tag{2}$$

in which the eigenvalues ω_j^2 ($j = 1, \ldots, n_{\mathrm{dof}}$) are the square of the natural frequencies $\omega_j \in \mathbb{R}$ and the eigenvectors $\boldsymbol{\phi}_j \in \mathbb{R}^{n_{\mathrm{dof}}}$ are the mode shapes. In any case, the displacement vector $\mathbf{u}(t)$ can be decomposed in n_{dof} contributions of the eigenmodes, also known as modal decomposition [35]:

$$\mathbf{u}(t) = \sum_{j=1}^{n_{\mathrm{dof}}} \boldsymbol{\phi}_j z_j(t) \tag{3}$$

where $z_j(t)$ represents the modal coordinate corresponding to mode j. In many applications, only a limited number of modes (n_{m} modes) significantly contribute to the response of the structure within the frequency band of interest. The remaining modes ($n_{\mathrm{dof}} - n_{\mathrm{m}}$ modes) are generally omitted, hereby allowing for model order reduction.

In the special case of proportional damping, the mode shapes $\boldsymbol{\phi}_j$ after mass normalization diagonalize the mass, damping, and stiffness matrix as follows:

$$\begin{aligned} \boldsymbol{\phi}_i^{\mathrm{T}} \mathbf{M} \boldsymbol{\phi}_j &= \delta_{[i-j]} \\ \boldsymbol{\phi}_i^{\mathrm{T}} \mathbf{C} \boldsymbol{\phi}_j &= 2\xi_j \omega_j \delta_{[i-j]} \\ \boldsymbol{\phi}_i^{\mathrm{T}} \mathbf{K} \boldsymbol{\phi}_j &= \omega_j^2 \delta_{[i-j]} \end{aligned} \tag{4}$$

where ξ_j is the damping ratio corresponding to mode j and $\delta_{[k]} = 1$ for $k = 0$ and 0 otherwise. The diagonalization originates from the orthogonality of the mode shape vectors with respect to the matrices $\mathbf{M}$, $\mathbf{C}$, and $\mathbf{K}$. Substitution of Eq. (3) in Eq. (1), subsequent left multiplication by the matrix $\boldsymbol{\Phi}^{\mathrm{T}}$, with $\boldsymbol{\Phi} \in \mathbb{R}^{n_{\mathrm{dof}} \times n_{\mathrm{m}}}$ containing the n_{m} mass-normalized mode shapes $\boldsymbol{\phi}_j$ as columns, and taking into account Eq. (4), yields the following continuous-time decoupled equations of motion in modal coordinates:

$$\ddot{\mathbf{z}}(t) + \boldsymbol{\Gamma}\dot{\mathbf{z}}(t) + \boldsymbol{\Omega}^2 \mathbf{z}(t) = \boldsymbol{\Phi}^{\mathrm{T}} \mathbf{S}_{\mathrm{p}}(t) \mathbf{p}(t) \tag{5}$$

where $\mathbf{z}(t) \in \mathbb{R}^{n_{\mathrm{m}}}$ is the vector of modal coordinates, with n_{m} the number of modes taken into account in the model. $\boldsymbol{\Gamma} \in \mathbb{R}^{n_{\mathrm{m}} \times n_{\mathrm{m}}}$ is a diagonal matrix containing the terms $2\xi_j\omega_j$ on its diagonal. $\boldsymbol{\Omega} \in \mathbb{R}^{n_{\mathrm{m}} \times n_{\mathrm{m}}}$ is a diagonal matrix as well, containing the natural frequencies ω_j on its diagonal.

The output vector is generally written as:

$$\begin{aligned} \mathbf{d}(t) &= \mathbf{S}_{\mathrm{d,a}} \ddot{\mathbf{u}}(t) + \mathbf{S}_{\mathrm{d,v}} \dot{\mathbf{u}}(t) + \mathbf{S}_{\mathrm{d,d}} \mathbf{u}(t) \\ &= \mathbf{S}_{\mathrm{d,a}} \boldsymbol{\Phi} \ddot{\mathbf{z}}(t) + \mathbf{S}_{\mathrm{d,v}} \boldsymbol{\Phi} \dot{\mathbf{z}}(t) + \mathbf{S}_{\mathrm{d,d}} \boldsymbol{\Phi} \mathbf{z}(t) \end{aligned} \tag{6}$$

where $\mathbf{S}_{\mathrm{d,a}}$, $\mathbf{S}_{\mathrm{d,v}}$, and $\mathbf{S}_{\mathrm{d,d}} \in \mathbb{R}^{n_{\mathrm{d}} \times n_{\mathrm{dof}}}$ are selection matrices indicating the degrees of freedom corresponding to the n_{d} acceleration, velocity, and displacement (or strain) measurements, respectively.

Eqs. (5) and (6) can be written into state-space form. After time discretization and accounting for process as well as measurement noise, the following discrete-time combined deterministic-stochastic state-space description of the system is obtained:

$$\mathbf{x}_{[k+1]} = \mathbf{A}\mathbf{x}_{[k]} + \mathbf{B}\mathbf{p}_{[k]} + \mathbf{w}_{[k]} \tag{7}$$

$$\mathbf{d}_{[k]} = \mathbf{G}\mathbf{x}_{[k]} + \mathbf{J}\mathbf{p}_{[k]} + \mathbf{v}_{[k]} \tag{8}$$

where $\mathbf{x}_{[k]} = \mathbf{x}(k\Delta t)$ and $\mathbf{p}_{[k]} = \mathbf{p}(k\Delta t)$, and $\mathbf{d}_{[k]} = \mathbf{d}(k\Delta t)$ $(k = 0, \ldots, N-1)$, Δt is the sampling time step, and N is the total number of samples.The state vector $\mathbf{x}_{[k]} \in \mathbb{R}^{n_\mathrm{s}}$ consists of the modal displacements and velocities: $\mathbf{x}_{[k]} = \begin{bmatrix} \mathbf{z}_{[k]}^\mathrm{T} & \dot{\mathbf{z}}_{[k]}^\mathrm{T} \end{bmatrix}^\mathrm{T}$, with n_s $(= 2n_\mathrm{m})$ the number of system states. The process noise $\mathbf{w}_{[k]}$ accounts for modeling errors and unknown stochastic excitation, i.e. excitation which is not accounted for by the excitation force in Eq. (5). The measurement noise $\mathbf{v}_{[k]}$ accounts for modeling errors, unknown stochastic excitation, and measurement errors. The expressions for the system matrices $\mathbf{A}$, $\mathbf{B}$, $\mathbf{G}$, and $\mathbf{J}$ for modally reduced order models and full order models can be found in [32]. Alternatively, the system matrices can be directly identified from experimental vibration data using system identification techniques, see e.g. [36, 37].

Finally, consider a vector $\mathbf{d}_\mathrm{e}(t) \in \mathbb{R}^{n_\mathrm{de}}$ of n_de outputs that are extrapolated from the measured data and the system model:

$$\mathbf{d}_\mathrm{e}(t) = \mathbf{S}_\mathrm{de,a}\mathbf{\Phi}\ddot{\mathbf{z}}(t) + \mathbf{S}_\mathrm{de,v}\mathbf{\Phi}\dot{\mathbf{z}}(t) + \mathbf{S}_\mathrm{de,d}\mathbf{\Phi}\mathbf{z}(t) \tag{9}$$

where the matrices $\mathbf{S}_\mathrm{de,a}$, $\mathbf{S}_\mathrm{de,v}$, and $\mathbf{S}_\mathrm{de,d} \in \mathbb{R}^{n_\mathrm{de} \times n_\mathrm{dof}}$ relate the identified accelerations, velocities and displacements or strains, respectively, to the degrees of freedom in the model (see also Eq. (6)). In the particular case of strain estimation as considered in this paper, the selection matrices $\mathbf{S}_\mathrm{de,a}$ and $\mathbf{S}_\mathrm{de,v}$ equal zero. After transformation of Eq. (9) into its state-space form, using Eq. (5), and adding measurement noise, the following (discrete-time) output equation corresponding to the extrapolated output quantities is obtained:

$$\mathbf{d}_{\mathrm{e}[k]} = \mathbf{G}_\mathrm{e}\mathbf{x}_{[k]} + \mathbf{J}_\mathrm{e}\mathbf{p}_{[k]} + \mathbf{v}_{\mathrm{e}[k]} \tag{10}$$

The matrices $\mathbf{G}_\mathrm{e} \in \mathbb{R}^{n_\mathrm{de} \times n_\mathrm{s}}$ and $\mathbf{J}_\mathrm{e} \in \mathbb{R}^{n_\mathrm{de} \times n_\mathrm{p}}$ relate to the extrapolated output quantities and therefore are different from the original matrices $\mathbf{G}$ and $\mathbf{J}$ in Eq. (8), that correspond to the measured output quantities. Note that in case of strain estimation, the direct feedthrough matrix $\mathbf{J}_\mathrm{e}$ equals zero. The measurement noise $\mathbf{v}_{\mathrm{e}[k]}$ accounts for modeling errors and unknown stochastic excitation.

2.2. Kalman filter algorithm

The Kalman filter [38] is a state estimation algorithm. The system states are estimated from a limited number of response measurements (e.g. accelerations) and a system model. In the derivation of the Kalman filter, the unknown system input is assumed to be zero mean white noise and is included in the noise processes $\mathbf{w}_{[k]}$ and $\mathbf{v}_{[k]}$. Under this assumption, the system described by Eqs. (7) and (8) becomes:

$$\mathbf{x}_{[k+1]} = \mathbf{A}\mathbf{x}_{[k]} + \mathbf{w}_{[k]} \tag{11}$$

$$\mathbf{d}_{[k]} = \mathbf{G}\mathbf{x}_{[k]} + \mathbf{v}_{[k]} \tag{12}$$

The noise processes $\mathbf{w}_{[k]}$ and $\mathbf{v}_{[k]}$, which now account for all excitation sources, are assumed to be zero mean and white, with known covariance matrices $\mathbf{Q}$, $\mathbf{R}$, and $\mathbf{S}$:

$$\mathbb{E}\left[\begin{pmatrix} \mathbf{w}_{[k]} \\ \mathbf{v}_{[k]} \end{pmatrix} \begin{pmatrix} \mathbf{w}_{[l]}^\mathrm{T} & \mathbf{v}_{[l]}^\mathrm{T} \end{pmatrix}\right] = \begin{bmatrix} \mathbf{Q} & \mathbf{S} \\ \mathbf{S}^\mathrm{T} & \mathbf{R} \end{bmatrix} \delta_{[k-l]} \tag{13}$$

with $\mathbf{R} > 0$, $\begin{bmatrix} \mathbf{Q} & \mathbf{S} \\ \mathbf{S}^\mathrm{T} & \mathbf{R} \end{bmatrix} \geq 0$, and $\delta_{[k]} = 1$ for $k = 0$ and 0 otherwise.

State estimation consists of estimating the system states $\mathbf{x}_{[k]}$, from a set of response measurements $\mathbf{d}_{[k]}$. A state estimate $\hat{\mathbf{x}}_{[k|l]}$ is defined as an estimate of $\mathbf{x}_{[k]}$, given the output sequence $\mathbf{d}_{[n]}$, with $n = 0, 1, \ldots, l$. The corresponding error covariance matrix, denoted as $\mathbf{P}_{\mathrm{x}[k|l]}$, is defined as:

$$\mathbf{P}_{\mathrm{x}[k|l]} = \mathbb{E}\left\{(\mathbf{x}_{[k]} - \hat{\mathbf{x}}_{[k|l]})(\mathbf{x}_{[k]} - \hat{\mathbf{x}}_{[k|l]})^{\mathrm{T}}\right\} \tag{14}$$

The Kalman filter algorithm is initialized using an initial state estimate vector $\hat{\mathbf{x}}_{[0|-1]}$ and its error covariance matrix $\mathbf{P}_{\mathrm{x}[0|-1]}$, both assumed known. Hereafter, it propagates by computing state estimates $\hat{\mathbf{x}}_{[k+1|k]}$ recursively from the following equation:

$$\hat{\mathbf{x}}_{[k+1|k]} = \mathbf{A}\hat{\mathbf{x}}_{[k|k-1]} + \mathbf{K}_{[k]}\left(\mathbf{d}_{[k]} - \mathbf{G}\hat{\mathbf{x}}_{[k|k-1]}\right) \tag{15}$$

The gain matrix $\mathbf{K}_{[k]}$ is determined such that the state estimates are minimum variance and unbiased (i.e. $\mathbf{K}_{[k]} = \arg\min_{\mathbf{K}_{[k]}} \mathrm{tr}\left\{\mathbf{P}_{\mathrm{x}[k|k]}\right\}$, $\mathbb{E}\left\{\mathbf{x}_{[k]} - \hat{\mathbf{x}}_{[k|k]}\right\} = 0$). The recursive state estimator of the form (15) can be split in two steps, i.e. the measurement update and the time update:

Measurement update

$$\mathbf{L}_{[k]} = \mathbf{P}_{\mathrm{x}[k|k-1]}\mathbf{G}^{\mathrm{T}}\left(\mathbf{G}\mathbf{P}_{\mathrm{x}[k|k-1]}\mathbf{G}^{\mathrm{T}} + \mathbf{R}\right)^{-1} \tag{16}$$

$$\hat{\mathbf{x}}_{[k|k]} = \hat{\mathbf{x}}_{[k|k-1]} + \mathbf{L}_{[k]}\left(\mathbf{d}_{[k]} - \mathbf{G}\hat{\mathbf{x}}_{[k|k-1]}\right) \tag{17}$$

$$\mathbf{P}_{\mathrm{x}[k|k]} = \mathbf{P}_{\mathrm{x}[k|k-1]} - \mathbf{L}_{[k]}\mathbf{G}\mathbf{P}_{\mathrm{x}[k|k-1]} \tag{18}$$

with $\mathbf{K}_{[k]} = \mathbf{A}\mathbf{L}_{[k]}$.

Time update

$$\hat{\mathbf{x}}_{[k+1|k]} = \mathbf{A}\hat{\mathbf{x}}_{[k|k]} \tag{19}$$

$$\mathbf{P}_{\mathrm{x}[k+1|k]} = \mathbf{A}\mathbf{P}_{\mathrm{x}[k|k]}\mathbf{A}^{\mathrm{T}} + \mathbf{Q} - \mathbf{A}\mathbf{L}_{[k]}\mathbf{S}^{\mathrm{T}} - \mathbf{S}\mathbf{L}_{[k]}^{\mathrm{T}}\mathbf{A}^{\mathrm{T}} \tag{20}$$

The algorithm given in Eqs. (16) – (20) distinguishes itself from the classical Kalman filter by including the correlation between the process noise vector $\mathbf{w}_{[k]}$ and the measurement noise vector $\mathbf{v}_{[k]}$, i.e. $\mathbf{S} \neq \mathbf{0}$. This correlation is inherently present for civil engineering applications, when accelerations are measured [39]. In the equations above, the system is assumed to be time-invariant. The algorithm can, however, also be applied to time-variant systems, resulting in system matrices $\mathbf{A}_{[k]}$ and $\mathbf{G}_{[k]}$ depending on the time step k.

After applying the Kalman filter algorithm, the estimated state vector $\hat{\mathbf{x}}_{[k|k]}$ can be used to estimate the response at any location in the structure, using the following modified output equation:

$$\hat{\mathbf{d}}_{\mathrm{e}[k|k]} = \mathbf{G}_{\mathrm{e}}\hat{\mathbf{x}}_{[k|k]} \tag{21}$$

where $\hat{\mathbf{d}}_{\mathrm{e}[k|k]}$ is the estimated response vector. For acceleration estimation, an error is introduced when applying Eq. (21), since the direct feedthrough of the excitation as contained in the noise vectors $\mathbf{w}_{[k]}$ and $\mathbf{v}_{[k]}$ is disregarded in the response estimation step.

2.3. Joint input-state estimation algorithm

The objective of joint input-state estimation is to jointly estimate the forces on the structure and the corresponding states from a limited number of response measurements and a system

model. The algorithm outlined next is a joint input-state estimation algorithm which was originally proposed by Gillijns and De Moor in [31] and further extended in [34] to account for the correlation between the process noise $\mathbf{w}_{[k]}$ and measurement noise $\mathbf{v}_{[k]}$. This correlation must be accounted for when the data vector $\mathbf{d}_{[k]}$ includes acceleration and the structure is subjected to unknown stochastic excitation [39]. The algorithm proposed in [34] is briefly summarized here for the sake of completeness.

The system under consideration is described by Eqs. (7) and (8). The noise processes $\mathbf{w}_{[k]}$ and $\mathbf{v}_{[k]}$ are assumed to be zero mean and white, with known covariance matrices $\mathbf{Q}$, $\mathbf{R}$, and $\mathbf{S}$, defined by Eq. (13). Throughout the derivation of the algorithm, it is assumed that the sensor network meets the conditions for instantaneous system inversion derived in [40]. Joint input-state estimation consists of estimating the forces $\mathbf{p}_{[k]}$ and states $\mathbf{x}_{[k]}$, from a set of response measurements $\mathbf{d}_{[k]}$. A state estimate $\hat{\mathbf{x}}_{[k|l]}$ is defined as an estimate of $\mathbf{x}_{[k]}$, given the output sequence $\mathbf{d}_{[n]}$, with $n = 0, 1, \ldots, l$. The corresponding error covariance matrix, denoted as $\mathbf{P}_{\mathrm{x}[k|l]}$, is defined in Eq. (14). An input estimate $\hat{\mathbf{p}}_{[k|l]}$ and its error covariance matrix $\mathbf{P}_{\mathrm{p}[k|l]}$ are defined similarly. The cross covariance matrices $\mathbf{P}_{\mathrm{xp}[k|l]}$ and $\mathbf{P}_{\mathrm{px}[k|l]}$ are defined as:

$$\mathbf{P}_{\mathrm{xp}[k|l]} = \mathbf{P}_{\mathrm{px}[k|l]}^{\mathrm{T}} := \mathbb{E}\left\{(\mathbf{x}_{[k]} - \hat{\mathbf{x}}_{[k|l]})(\mathbf{p}_{[k]}^{\mathrm{T}} - \hat{\mathbf{p}}_{[k|l]}^{\mathrm{T}})\right\} \tag{22}$$

The filtering algorithm is initialized using an initial state estimate vector $\hat{\mathbf{x}}_{[0|-1]}$ and its error covariance matrix $\mathbf{P}_{\mathrm{x}[0|-1]}$. The algorithm proceeds by computing the force and state estimates recursively in three steps, i.e. the input estimation step, the measurement update and the time update:

Input estimation

$$\tilde{\mathbf{R}}_{[k]} = \mathbf{G}\mathbf{P}_{\mathrm{x}[k|k-1]}\mathbf{G}^{\mathrm{T}} + \mathbf{R} \tag{23}$$

$$\mathbf{M}_{[k]} = \left(\mathbf{J}^{\mathrm{T}}\tilde{\mathbf{R}}_{[k]}^{-1}\mathbf{J}\right)^{-1}\mathbf{J}^{\mathrm{T}}\tilde{\mathbf{R}}_{[k]}^{-1} \tag{24}$$

$$\hat{\mathbf{p}}_{[k|k]} = \mathbf{M}_{[k]}\left(\mathbf{d}_{[k]} - \mathbf{G}\hat{\mathbf{x}}_{[k|k-1]}\right) \tag{25}$$

$$\mathbf{P}_{\mathrm{p}[k|k]} = \left(\mathbf{J}^{\mathrm{T}}\tilde{\mathbf{R}}_{[k]}^{-1}\mathbf{J}\right)^{-1} \tag{26}$$

Measurement update

$$\mathbf{K}_{[k]} = \mathbf{P}_{\mathrm{x}[k|k-1]}\mathbf{G}^{\mathrm{T}}\tilde{\mathbf{R}}_{[k]}^{-1} \tag{27}$$

$$\hat{\mathbf{x}}_{[k|k]} = \hat{\mathbf{x}}_{[k|k-1]} + \mathbf{K}_{[k]}\left(\mathbf{d}_{[k]} - \mathbf{G}\hat{\mathbf{x}}_{[k|k-1]} - \mathbf{J}\hat{\mathbf{p}}_{[k|k]}\right) \tag{28}$$

$$\mathbf{P}_{\mathrm{x}[k|k]} = \mathbf{P}_{\mathrm{x}[k|k-1]} - \mathbf{K}_{[k]}\left(\tilde{\mathbf{R}}_{[k]} - \mathbf{J}\mathbf{P}_{\mathrm{p}[k|k]}\mathbf{J}^{\mathrm{T}}\right)\mathbf{K}_{[k]}^{\mathrm{T}} \tag{29}$$

$$\mathbf{P}_{\mathrm{xp}[k|k]} = \mathbf{P}_{\mathrm{px}[k|k]}^{\mathrm{T}} = -\mathbf{K}_{[k]}\mathbf{J}\mathbf{P}_{\mathrm{p}[k|k]} \tag{30}$$

Time update

$$\hat{\mathbf{x}}_{[k+1|k]} = \mathbf{A}\hat{\mathbf{x}}_{[k|k]} + \mathbf{B}\hat{\mathbf{p}}_{[k|k]} \tag{31}$$

$$\mathbf{N}_{[k]} = \mathbf{A}\mathbf{K}_{[k]}\left(\mathbf{I}_{n_{\mathrm{d}}} - \mathbf{J}\mathbf{M}_{[k]}\right) + \mathbf{B}\mathbf{M}_{[k]} \tag{32}$$

$$\mathbf{P}_{\mathrm{x}[k+1|k]} = \begin{bmatrix}\mathbf{A} & \mathbf{B}\end{bmatrix}\begin{bmatrix}\mathbf{P}_{\mathrm{x}[k|k]} & \mathbf{P}_{\mathrm{xp}[k|k]} \\ \mathbf{P}_{\mathrm{px}[k|k]} & \mathbf{P}_{\mathrm{p}[k|k]}\end{bmatrix}\begin{bmatrix}\mathbf{A}^{\mathrm{T}} \\ \mathbf{B}^{\mathrm{T}}\end{bmatrix} + \mathbf{Q} - \mathbf{N}_{[k]}\mathbf{S}^{\mathrm{T}} - \mathbf{S}\mathbf{N}_{[k]}^{\mathrm{T}} \tag{33}$$

The gain matrices $\mathbf{M}_{[k]}$ and $\mathbf{L}_{[k]}$ are determined such that both the input estimates $\hat{\mathbf{p}}_{[k|k]}$ and the state estimates $\hat{\mathbf{x}}_{[k|k-1]}$ are minimum variance and unbiased [31]. In the equations above, the system is assumed to be time-invariant. The algorithm can, however, also be applied to time-variant systems, resulting in system matrices $\mathbf{A}_{[k]}$, $\mathbf{B}_{[k]}$, $\mathbf{G}_{[k]}$, and $\mathbf{J}_{[k]}$ depending on the time step k.

Very often unknown forces such as wind loads are acting on the structure. For these loads, the force locations or spatial distributions are not well known. In this case, the estimated forces $\mathbf{p}_{[k]}$ compensate for any unknown source of vibration and an attempt is made to identify equivalent forces instead of the true forces acting on the structure.

After applying the joint input-state estimation algorithm, the estimated state vector $\hat{\mathbf{x}}_{[k|k]}$ and force vector $\hat{\mathbf{p}}_{[k|k]}$ can be used to estimate the output at any location in the structure, using the following modified output equation:

$$\hat{\mathbf{d}}_{\mathrm{e}[k|k]} = \mathbf{G}_{\mathrm{e}}\hat{\mathbf{x}}_{[k|k]} + \mathbf{J}_{\mathrm{e}}\hat{\mathbf{p}}_{[k|k]} \tag{34}$$

In the particular case of strain estimation as considered in this paper, the direct feedthrough matrix $\mathbf{J}_{\mathrm{e}}$ equals zero and only the estimated state vector $\hat{\mathbf{x}}_{[k|k]}$ is used in the estimation.

2.4. Modal expansion algorithm

Modal expansion is a well known technique in modal analysis, a.k.a. full-field strain measurements. The approach consist of two steps. The first step is a modal decomposition of the measured outputs $\mathbf{d}(t)$ into the contributions of the modes contained in the matrix $\mathbf{\Phi}$. If only accelerations are measured, $\mathbf{S}_{\mathrm{d,v}}$ and $\mathbf{S}_{\mathrm{d,d}}$ both equal to zero and Eq. (6) reduces to:

$$\mathbf{d}(t) = \mathbf{S}_{\mathrm{d,a}}\mathbf{\Phi}\ddot{\mathbf{z}}(t) \tag{35}$$

Eq. (35) can be solved at each time instance t for the modal accelerations $\hat{\ddot{\mathbf{z}}}(t)$:

$$\hat{\ddot{\mathbf{z}}}(t) = \left(\mathbf{S}_{\mathrm{d,a}}\mathbf{\Phi}\right)^{\dagger}\mathbf{d}(t) \tag{36}$$

where $\bullet^{\dagger}$ is the Moore-Penrose pseudo-inverse. When the number of modes n_{m} matches the number of measured outputs n_{d}, Eq. (36) is solved as a determined system. When n_{d} exceeds n_{m}, Eq. (36) is solved as an overdetermined system.
The modal decomposition can also be adapted to allow for different output quantities, e.g. to use both acceleration and strain measurements. This is done by converting all output measurements to displacements $\mathbf{d}'(t)$, e.g. through (double) integration of the accelerations, and solving Eq. (36) for modal displacements $\hat{\mathbf{z}}(t)$. In order to accommodate for differences in order of magnitude and the signal-to-noise-ratio between different output quantities in $\mathbf{d}'(t)$, the error covariance matrix $\mathbf{R}_{\mathrm{M}} \in \mathbb{R}^{n_{\mathrm{d}} \times n_{\mathrm{d}}}$ is accounted for in the estimation as follows:

$$\hat{\mathbf{z}}(t) = \left(\mathbf{R}_{\mathrm{M}}^{-1/2}\mathbf{S}_{\mathrm{d,d}}\mathbf{\Phi}\right)^{\dagger}\left(\mathbf{R}_{\mathrm{M}}^{-1/2}\mathbf{d}'(t)\right) \tag{37}$$

Alternatively, the decomposition can also be performed in the frequency domain, taking the Fourier transform of Eq. (6) and solving for the modal displacements $\hat{\mathbf{Z}}(\omega)$:

$$\hat{\mathbf{Z}}(\omega) = \left(-\omega^2\mathbf{R}_{\mathrm{M}}^{-1/2}\mathbf{S}_{\mathrm{d,a}}\mathbf{\Phi} + i\omega\mathbf{R}_{\mathrm{M}}^{-1/2}\mathbf{S}_{\mathrm{d,v}}\mathbf{\Phi} + \mathbf{R}_{\mathrm{M}}^{-1/2}\mathbf{S}_{\mathrm{d,d}}\mathbf{\Phi}\right)^{\dagger}\left(\mathbf{R}_{\mathrm{M}}^{-1/2}\mathbf{D}(\omega)\right) \tag{38}$$

where $\mathbf{D}(\omega)$ is the Fourier transform of the output vector $\mathbf{d}(t)$. While this frequency domain implementation is equivalent to its time domain counterpart, it is a more elegant solution in case

of different output quantities.
The second step of modal expansion uses Eq. (9) and for instance the estimated modal accelerations $\hat{\ddot{\mathbf{z}}}(t)$ obtained from Eq. (36), in order to obtain the extrapolated output quantities $\hat{\mathbf{d}}_{\mathrm{e}}(t)$:

$$\hat{\mathbf{d}}_{\mathrm{e}}(t) = \mathbf{S}_{\mathrm{d_e,a}}\boldsymbol{\Phi}\hat{\ddot{\mathbf{z}}}(t) + \mathbf{S}_{\mathrm{d_e,v}}\boldsymbol{\Phi}\mathcal{F}^{-1}\left\{\frac{1}{i\omega}\mathcal{F}\left\{\hat{\ddot{\mathbf{z}}}(t)\right\}\right\} + \mathbf{S}_{\mathrm{d_e,d}}\boldsymbol{\Phi}\mathcal{F}^{-1}\left\{\frac{1}{-\omega^2}\mathcal{F}\left\{\hat{\ddot{\mathbf{z}}}(t)\right\}\right\} \tag{39}$$

where $\mathcal{F}\{\bullet\}$ and $\mathcal{F}^{-1}\{\bullet\}$ denote the Fourier transform and the inverse Fourier transform, respectively. Eq. (39) integrates the estimated modal accelerations to modal velocities and modal displacements through the frequency domain, but a time-domain implementation is also possible. Note that, if one wishes to solely predict accelerations, the modal decomposition and expansion can be easily performed in real-time, as $\mathbf{S}_{\mathrm{d_e,v}}$ and $\mathbf{S}_{\mathrm{d_e,d}}$ equal zero. This was demonstrated on the same offshore wind turbine in [19].
For the current application, in which accelerations are used to predict strains, Eq. (39) reduces to:

$$\hat{\mathbf{d}}_{\mathrm{e}}(t) = \mathbf{S}_{\mathrm{d_e,d}}\boldsymbol{\Phi}\mathcal{F}^{-1}\left\{\frac{1}{-\omega^2}\mathcal{F}\left\{\hat{\ddot{\mathbf{z}}}(t)\right\}\right\} \tag{40}$$

Integration of the modal accelerations is required as strain is related to modal displacements. An interesting property of the modal expansion algorithm is that it does not require knowledge of the structure's natural frequencies and damping ratios, and only relies on the mode shapes of the structure for response estimation. This is a clear advantage, as the natural frequencies and damping ratios of (offshore) wind turbines vary strongly with operational and environmental conditions [41, 42]. Note that the Kalman filter algorithm and the joint input-state estimation algorithm rely on all modal properties. For small variations of the natural frequencies and damping ratios, however, the response estimates are only marginally affected, as illustrated in [43]. The impact of the variability of the natural frequencies over time in this particular application is still to be analyzed using a long-term data set.

3. Monopile wind turbine

In this section, the response estimation algorithms proposed in Section 2 are applied for a data set obtained from a monitoring campaign on a Vestas V90 3 MW wind turbine on a monopile foundation (Fig. 1) [30]. The wind turbine is located at the Belwind offshore windfarm in the North Sea, 46 km off the Belgian coast. The hub-height of the wind turbine is on average located at 72 m above the lowest astronomical tide (LAT). The wind turbine is mounted on a monopile foundation with a diameter of 5 m. The water depth at the turbine location is 24 m w.r.t. LAT and the monopile has a penetration depth of 21 m.

(a) 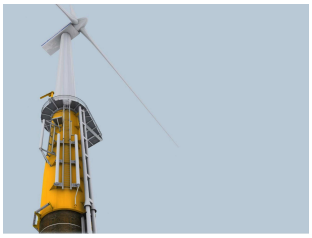 (b) 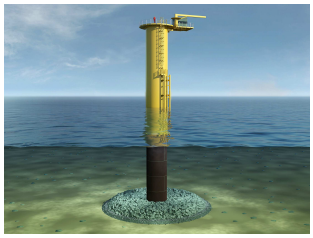

Fig. 1: (a) Vestas V90 3 MW wind turbine on a monopile foundation and (b) mud-line, hotspot for fatigue assessment.

3.1. Measurement setup

The measurement data consist of eight data sets with a duration of 10 minutes each. Data sets 1 – 4 correspond to rotating conditions of the turbine (wind speed ±11 m/s, rotation speed turbine ±16 rpm), data sets 5 – 8 correspond to parked conditions of the turbine (wind speed ±2 m/s, rotation speed turbine <1 rpm).

In total, 10 accelerometers and 6 strain gauges have been installed on the wind turbine; 4 accelerometers at a height of 69 m (LAT), 2 accelerometers and 2 optical fiber bragg grating strain sensors at a height of 41 m (LAT), 2 accelerometers at a height of 27 m (LAT), and 2 accelerometers and 4 optical fiber bragg grating strain sensors at a height of 19 m (LAT). Fig. 2 shows the sensor configuration. The data at all levels are transformed in respectively the Fore-Aft (FA) direction and the Side-Side (SS) direction using the known yaw direction. FA motion is parallel to the wind direction and SS motion is perpendicular to the wind direction. The acceleration and strain data obtained are hereafter referred to as $a_{\alpha\beta}$ and $\epsilon_{\alpha\beta}$, respectively, where α indicates the level in m LAT and β indicates the direction (FA or SS).

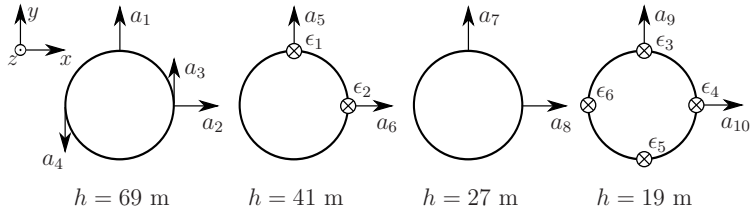

Fig. 2: Sensor configuration (levels h relative to LAT).

3.2. Data acquisition and processing

A sampling rate of 20 Hz is used in the data acquisition. For each data block of 10 minutes, the frequency content below 0.05 Hz and above 5 Hz has been removed. As an example, the processed acceleration and strain data at level $h = 41$ m LAT (FA and SS) are shown in Figs. 3 and 4 for data set 1 (rotating conditions) and in Figs. 5 and 6 for data set 5 (parked conditions). The sample Power Spectral Density (PSD) function is estimated using Welch's method, hereby applying a window length of 1024 samples and an overlap of 66%. Whereas for rotating conditions (Figs. 3 and 4) all modes in the frequency range from 0 to 5 Hz have a significant contribution to the measured response, the response for parked conditions (Figs. 5 and 6) is mainly dominated by the first mode (FA and SS). It is also clearly seen in Fig. 6b that the measured strains for parked conditions (low excitation levels) hit the noise floor of the strain gauges beyond the first mode, i.e. for frequencies higher than ±0.9 Hz. For the acceleration data, the observed peaks in the PSD (Fig. 5b) correspond to known natural frequencies of the structure (see also Section 3.3). In the frequency range from 1 to 5 Hz, the signal in between these peaks consists of measurement noise, as the acceleration signal hits the noise floor of the sensor.

3.3. System model

A system model is constructed from a FE model of the wind turbine, developed by OWI/VUB. The FE model has been updated using a set of experimental modal parameters, which have been obtained through an output-only system identification procedure using data collected in parked conditions [19, 44]. The displacement mode shapes corresponding to the first six modes calculated using the updated FE model are shown in Fig. 7. Table 1 shows the experimentally identified

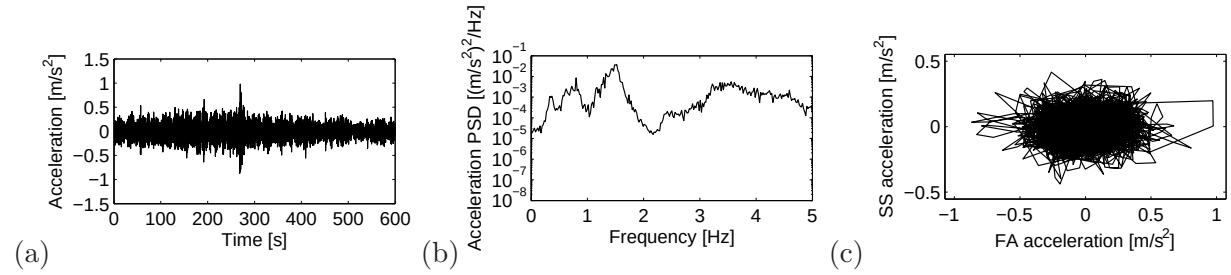

Fig. 3: (a) Time history and (b) estimated PSD of the FA acceleration measured at level $h = 41$ m LAT for **data set 1** (rotating conditions), and (c) time history of the FA acceleration versus time history of the SS acceleration measured at level $h = 41$ m LAT.

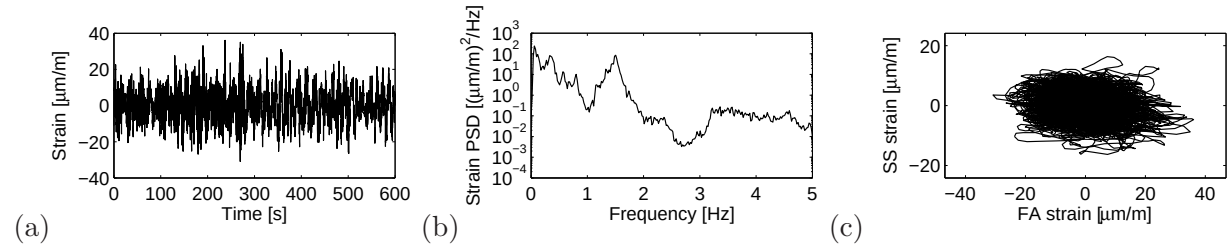

Fig. 4: (a) Time history and (b) estimated PSD of the FA strain measured at level $h = 41$ m LAT for **data set 1** (rotating conditions), and (c) time history of the FA strain versus time history of the SS strain measured at level $h = 41$ m LAT.

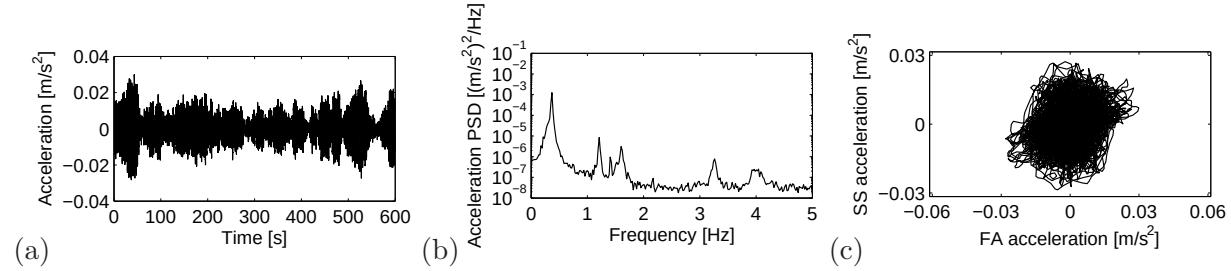

Fig. 5: (a) Time history and (b) estimated PSD of the FA acceleration measured at level $h = 41$ m LAT for **data set 5** (parked conditions), and (c) time history of the FA acceleration versus time history of the SS acceleration measured at level $h = 41$ m LAT.

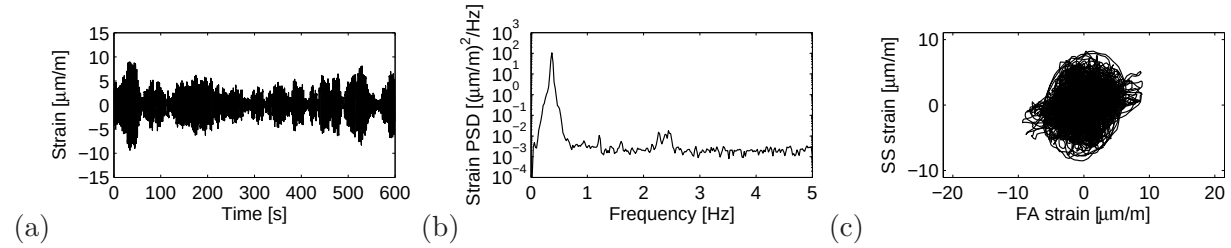

Fig. 6: (a) Time history and (b) estimated PSD of the FA strain measured at level $h = 41$ m LAT for **data set 5** (parked conditions), and (c) time history of the FA strain versus time history of the SS strain measured at level $h = 41$ m LAT.

natural frequencies and modal damping ratios [44], as well as the natural frequencies obtained from the FE model and the MAC-values, which indicate the agreement between the measured and computed displacement mode shapes [45]. For nearly all bending modes of the wind turbine, a high MAC-value is obtained. Note that the FE model is symmetric, whereas the actual behavior of the wind turbine is different in the FA and SS directions and will vary for different wind directions [46].

A reduced-order discrete-time state-space model is constructed from the FE model of the wind turbine, applying a zero order hold assumption on the force. The model includes the 6 modes listed in Table 1. For each mode, the mass normalized mode shape and natural frequency are assumed to be known from the FE model, whereas the modal damping ratio is taken as the experimentally identified value. The state-space model is used for the application of the Kalman filter algorithm and the joint input-state estimation algorithm. For the modal expansion algorithm, the mode shapes of the 6 modes listed in Table 1 are included in the estimation.

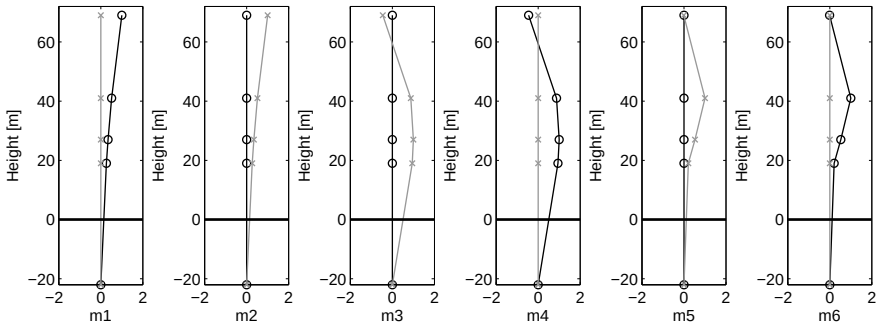

Fig. 7: First six displacement mode shapes obtained from the FE model, FA-direction (black) and SS-direction (gray). From left to right: FA1, SS1, SS2, FA2, SS3, FA3.

No.	f_{id} [Hz]	f_{fem} [Hz]	ξ_{id} [%]	MAC	Description
1	0.361	0.374	1.86	0.99	First FA bending mode
2	0.365	0.374	2.49	0.99	First SS bending mode
3	1.448	1.440	1.38	0.99	Second SS bending mode
4	1.560	1.440	1.14	0.98	Second FA bending mode
5	3.610	3.636	0.56	0.96	Third SS bending mode
6	3.910	3.636	0.92	0.92	Third FA bending mode

Table 1: Experimentally identified modal characteristics and comparison to the modal characteristics obtained from the FE model (f_{id}: identified natural frequency, f_{fem}: natural frequency obtained from FE model, ξ_{id}: identified modal damping ratio, MAC: MAC-value [45]).

3.4. Verification using measured data

The applicability of the response estimation algorithms introduced in Section 2 is now verified by predicting the FA and SS strain at the lowest measurement level ($h = 19$ m LAT). Two sensor configurations are compared, hereafter referred to as S_1 and S_2. Sensor configuration S_1 consists of six accelerations ($a_{69\mathrm{FA}}$, $a_{69\mathrm{SS}}$, $a_{41\mathrm{FA}}$, $a_{41\mathrm{SS}}$, $a_{27\mathrm{FA}}$, $a_{27\mathrm{SS}}$). Sensor configuration S_2 consists of the same six accelerations and in addition contains two strains at level $h = 41$ m LAT ($\epsilon_{41\mathrm{FA}}$ and $\epsilon_{41\mathrm{SS}}$).

The force vector $\mathbf{p}_{[k]}$ assumed for joint input-state estimation consist of six independent modal forces. For the stability of the joint input-state estimation algorithm and the uniqueness of the estimated quantities, at least n_{p} displacements or strains are required as part of the output vector $\mathbf{d}_{[k]}$, in addition to the measured accelerations [40], where n_{p} is the number of forces ($n_{\mathrm{p}} = 6$). In this analysis, no displacements have been measured and a set of displacements is calculated by (offline) numerical integration of the acceleration data. The signals obtained by integration have

been highpass filtered applying a cutoff frequency of 0.25 Hz. The aim of the filter is to remove the low frequency components from the signals which are contaminated by measurement noise. Six displacements are added to both data sets S_1 and S_2 used for joint input-state estimation ($d_{69\mathrm{FA}}$, $d_{69\mathrm{SS}}$, $d_{41\mathrm{FA}}$, $d_{41\mathrm{SS}}$, $d_{27\mathrm{FA}}$, $d_{27\mathrm{SS}}$). The displacements obtained by integration have not been used for the application of the Kalman filter and the modal expansion algorithm.

The noise covariance matrices $\mathbf{Q}$, $\mathbf{R}$, and $\mathbf{S}$ assumed for the application of the Kalman filter are calculated as:

$$\begin{bmatrix} \mathbf{Q} & \mathbf{S} \\ \mathbf{S}^{\mathrm{T}} & \mathbf{R} \end{bmatrix} = \begin{bmatrix} \mathbf{B}_{\mathrm{dof}} \\ \mathbf{J}_{\mathrm{dof}} \end{bmatrix} \mathbf{C}_{\mathrm{p}} \begin{bmatrix} \mathbf{B}_{\mathrm{dof}}^{\mathrm{T}} & \mathbf{J}_{\mathrm{dof}}^{\mathrm{T}} \end{bmatrix} + \begin{bmatrix} \mathbf{0} & \mathbf{0} \\ \mathbf{0} & \mathbf{R}_{\mathrm{M}} \end{bmatrix} \tag{41}$$

where $\mathbf{C}_{\mathrm{p}} \in \mathbb{R}^{n_{\mathrm{dof}} \times n_{\mathrm{dof}}}$ is the covariance matrix of the unknown system input and $\mathbf{R}_{\mathrm{M}} \in \mathbb{R}^{n_{\mathrm{d}} \times n_{\mathrm{d}}}$ is the measurement error covariance matrix, that act as tuning parameters/matrices. The system matrices $\mathbf{B}_{\mathrm{dof}} \in \mathbb{R}^{2n_{\mathrm{m}} \times n_{\mathrm{dof}}}$ and $\mathbf{J}_{\mathrm{dof}} \in \mathbb{R}^{n_{\mathrm{d}} \times n_{\mathrm{dof}}}$ are obtained by assuming $n_{\mathrm{p}} = n_{\mathrm{dof}}$ in Eqs. (7) and (8), respectively, i.e. excitation acting at every degree of freedom in the model. The matrix $\mathbf{R}_{\mathrm{M}}$ is assumed diagonal with values $(5 \times 10^{-4})^2$ $(\mathrm{m/s^2})^2$ and 0.15^2 $\mu\mathrm{s}^2$ for the diagonal elements corresponding to the accelerations and strains, respectively. The assigned values characterize the accuracy of the acceleration and strain sensors. The covariance matrix $\mathbf{C}_{\mathrm{p}}$ is chosen as $\sigma_{\mathrm{p_S}}^2 \times \mathbf{I}$. This corresponds to stochastic forces with a standard deviation $\sigma_{\mathrm{p_S}}$ acting in the FA and SS direction at the four levels where accelerations have been measured. The value of $\sigma_{\mathrm{p_S}}$ has been determined such that the uncertainty introduced by sensor noise and the (unknown) excitation is small, following the uncertainty quantification approach introduced in [34]. This approach has been previously applied for a case study in [47]. Fig. 8 shows the variation of the strain error variance with $\sigma_{\mathrm{p_S}}$, for both the FA and SS strain at level $h = 19$ m LAT and assuming sensor configuration S_2 in the strain estimation. The error variance is obtained considering the estimation errors in the frequency range from 0.25 to 5 Hz (see also [47]). It is observed that for lower values of $\sigma_{\mathrm{p_S}}$ ($< 10^4$ N) the error variance depends significantly on $\sigma_{\mathrm{p_S}}$. For larger values of $\sigma_{\mathrm{p_S}}$ ($> 10^4$ N), the error variance becomes low and independent on the value of $\sigma_{\mathrm{p_S}}$ assumed in the estimation. As observed from Fig. 8b, the error covariance obtained for $\sigma_{\mathrm{p_S}} \to \infty$ is not necessarily the minimum value, however. The value $\sigma_{\mathrm{p_S}} = 10^6$ N has been selected for strain estimation in the following, both for rotating and parked conditions, as it leads to low estimation uncertainty.

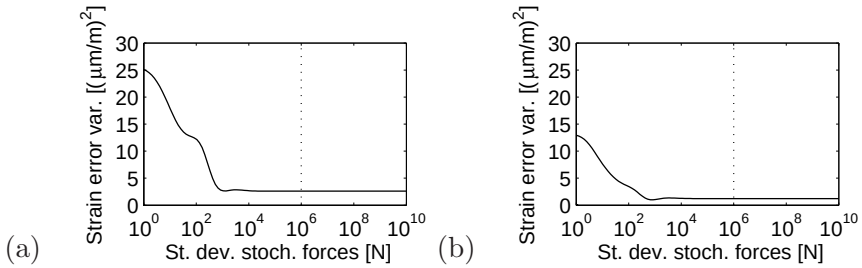

Fig. 8: Variance of the error on (a) the estimated FA strain and (b) the estimated SS strain at level $h = 19$ m LAT as a function of the standard deviation $\sigma_{\mathrm{p_S}}$ assumed for the application of the Kalman filter algorithm, sensor configuration S_2. The vertical dotted line indicates the value of $\sigma_{\mathrm{p_S}}$ selected for strain estimation in the following.

Since in the joint input-state estimation the equivalent forces are assumed to cover all excitation of the structure, the noise covariance matrices $\mathbf{Q}$, $\mathbf{R}$, and $\mathbf{S}$ assumed for the application of the joint input-state estimation algorithm are calculated from Eq. (41), with $\mathbf{C}_{\mathrm{p}} = \mathbf{0}$. The matrix $\mathbf{R}_{\mathrm{M}}$ is

assumed diagonal with values $(5\times10^{-4})^2$ $(\mathrm{m/s^2})^2$, 0.15^2 $\mu\mathrm{s}^2$, and 10^{-12} m^2 for the diagonal elements corresponding to the accelerations, strains, and displacements, respectively. The initial state vector $\hat{\mathbf{x}}_{[0|-1]}$ and the corresponding error covariance matrix $\mathbf{P}_{[0|-1]}$ are assumed zero in the application of both the Kalman filter and the joint input-state estimation algorithm.

The estimated strain signals obtained from the joint input-state estimation algorithm and the modal expansion algorithm are characterized by spurious low frequency components that originate from measurement noise on the acceleration data. The estimated strain signals obtained from both algorithms have therefore been highpass filtered applying a cutoff frequency of 0.25 Hz. The 0.25 Hz low frequency boundary is chosen to focus on dynamic strains. A further motivation is given in Section 3.5. The estimated strain signals obtained from the Kalman filter have not been filtered.

Figs. 9, 10, and 11 show the measured and estimated strain signals for data set 1 (rotating conditions) obtained from the Kalman filter, the joint input-state estimation algorithm, and the modal expansion algorithm, respectively, for sensor configuration S_1. The same highpass filter with a cutoff frequency of 0.25 Hz has been applied to the measured strain signals and the estimated strain signals obtained from the Kalman filter, before plotting the strain time histories. This allows for a fair comparison of the measured and estimated strains in the frequency interval from 0.25 to 5 Hz. The PSDs have been calculated from the original unfiltered data.
The results obtained from the joint input-state estimation algorithm (Fig. 10) and the modal expansion algorithm (Fig. 11) are very similar. Especially for the frequency range from 0.25 to 1 Hz, both algorithms yield better results than the Kalman filter. This is for example seen from comparison of Figs. 9c and 10c (FA strain), and Figs. 9f and 10f (SS strain). It is expected that the estimation errors for each of the algorithms mainly result from errors on the mode shapes (see also Section 2.4). The measured (unfiltered) strain signals are characterized by an important low frequency content (frequencies $<$ 0.25 Hz), which is not present in the estimated strain signals (see e.g. Figs. 9c and f). For the joint input-state estimation algorithm and the modal expansion algorithm, all low frequency oscillations have been removed by the highpass filter applied to the estimated strain signals (see also Section 3.5). For the Kalman filter, it is found that the low frequency information cannot be recovered from acceleration signals only (see for example Figs. 9c and f).

Figs. 12, 13, and 14 show the measured and estimated strain signals for data set 1 (rotating conditions) obtained from the Kalman filter, the joint input-state estimation algorithm, and the modal expansion algorithm, respectively, for sensor configuration S_2. Very accurate strain estimates are obtained from the three response estimation algorithms, both for the FA and SS direction. As indicated by Jo and Spencer in [24], the experimental validation shows that better strain estimates are obtained if the Kalman filter is fed with acceleration and strain data. This is seen from comparison of Figs. 9 and 12. Even more, it is observed from the PSD of the estimated strains obtained from the Kalman filter (Figs. 12c and f) that the Kalman filter provides accurate results in the quasi-static frequency range (frequencies $<$ 0.25 Hz) when strain data are included. For the joint input-state estimation algorithm and the modal expansion algorithm, the added value of including the strain signals is small. Most likely this is due to the dominance of higher order dynamics and rotor harmonics which are captured better in the measured accelerations than the mid-tower strain signals.

Figs. 15, 16, and 17 show the measured and estimated strain signals for data set 5 (parked conditions) obtained from the Kalman filter, the joint input-state estimation algorithm, and the

modal expansion algorithm, respectively, for sensor configuration S_1. The measured strain response for parked conditions is mainly dominated by the first bending mode, both for the FA and SS direction, as seen from the strain PSD. For frequencies between 0.3 and 0.6 Hz, there is a very good agreement between the measured strain signals and the strain signals obtained from the joint input-state estimation algorithm and the modal expansion algorithm (see Figs. 16c and f and Figs. 17c and f, respectively). For the Kalman filter algorithm, systematic errors are observed from both the time history and the PSD. It is expected that the estimation errors mainly result from errors on the mode shapes, and depend on the weighing of the response data in the estimation. It can clearly be seen how the measured strain signals (black) are hitting the noise floor of the strain gauges beyond the first mode at frequencies larger than 0.9 Hz. Interestingly, the predicted strains (colored) dive beneath the noise floor of the strain gauges. From the predicted strains, the noise floor of the accelerometers, multiplied with $1/\omega^2$ from the double integration, and following $1/\omega^4$ behavior in the PSD, is clearly visible at higher frequencies (see also Section 3.5). Higher order dynamics still appear in the predicted strain signals, however. The observed peaks, e.g. near 1.5 Hz, correspond to the natural frequencies given in Table 1. The peaks are not observed in the measured strains, since at the peak frequencies, the strains are below the noise level of the strain gauges.

Figs. 18, 19, and 20 show the measured and estimated strain signals for data set 5 (parked conditions) obtained from the Kalman filter, the joint input-state estimation algorithm, and the modal expansion algorithm, respectively, for sensor configuration S_2. For the Kalman filter, the estimated strains overestimate the measured strains (Fig. 18), whereas for sensor configuration S_1 the strains are generally underestimated. It is found that the Kalman filter assigns significant weight to the measured strain signals in the estimation. This is for example seen from the estimated strains for frequencies above 0.9 Hz. When only accelerations are accounted for (sensor configuration S_1, Figs. 15c and f), the PSD of the estimated strain signals shows the aforementioned $1/\omega^4$ behavior, as well as the peaks corresponding to the natural frequencies, which are contained in the acceleration data. When in addition strains are included in the data vector (sensor configuration S_2, Figs. 18c and f), the PSD amplitude of the estimated strain signals is larger over the entire frequency range from 0.9 to 5 Hz, and does not show clear peaks at the natural frequencies. The larger amplitude of the PSD originates from the noise floor of the strain sensors ($\epsilon_{41\mathrm{FA}}$ and $\epsilon_{41\mathrm{SS}}$), that becomes important at higher frequencies when large weight is assigned to the strains. For the joint input-state estimation algorithm and the modal expansion algorithm, the estimated strains are not significantly affected by the additional strain data.

In order to compare the quality of the strain estimates obtained from the three algorithms, two quality indicators are introduced. The first quality indicator is the Time Response Assurance Criterion (TRAC) [17], which is a measure for the overall correlation of the time history of the estimated strain signal ($\hat{\mathbf{d}}_{\mathrm{e}[k|k]}$) and the measured strain signal ($\mathbf{d}_{\mathrm{e}[k]}$) for one DOF:

$$\mathrm{TRAC} = \frac{\left(\sum_{l=0}^{N-1} \hat{\mathbf{d}}_{\mathrm{e}[l|l]} \mathbf{d}_{\mathrm{e}[l]}\right)^2}{\sum_{l=0}^{N-1} \hat{\mathbf{d}}_{\mathrm{e}[l|l]} \hat{\mathbf{d}}_{\mathrm{e}[l|l]} \sum_{l=0}^{N-1} \mathbf{d}_{\mathrm{e}[l]} \mathbf{d}_{\mathrm{e}[l]}} \tag{42}$$

The TRAC-value is a positive real quantity that takes values between zero and unity. Values close to unity indicate perfect agreement of the strain time histories, while significantly lower values indicate the presence of estimation errors.

The second quality indicator is the Mean Absolute Error (MAE) of the time history of the

estimated strain signal ($\hat{\mathbf{d}}_{\mathrm{e}[k|k]}$) with respect to the measured strain signal ($\mathbf{d}_{\mathrm{e}[k]}$) for one DOF:

$$\mathrm{MAE} = \frac{1}{N} \sum_{l=0}^{N-1} \left| \mathbf{d}_{\mathrm{e}[l]} - \hat{\mathbf{d}}_{\mathrm{e}[l|l]} \right| \tag{43}$$

Small MAE values (with respect to the actual strain magnitude) indicate a good agreement of the strain time histories.

Tables 2 and 3 show the TRAC and MAE values for rotating and parked conditions, respectively. The indicators have been obtained from the strain time histories after additional highpass filtering, applying a cutoff frequency of 0.25 Hz. This filtering is required to allow a proper comparison of the dynamic strains in the frequency range from 0.25 to 5 Hz.

For rotating conditions, it is clearly observed from both the TRAC and MAE values that the results obtained from the Kalman filter are significantly improved by including strain data (S_1: only acceleration data, S_2: acceleration and strain data). For the FA strain, the best results are obtained from the joint input-state estimation algorithm and the modal expansion algorithm (in rotating conditions). For the SS strain, the three algorithms yield comparable results when only acceleration data are included (sensor configuration S_1). When strain data are included (sensor configuration S_2), the most accurate results in this case are obtained from the Kalman filter.

For parked conditions, the Kalman filter algorithm outperforms the two remaining algorithms in terms of TRAC values. This indicates a high correlation between the measured and estimated strains. In terms of the MAE values, however, the Kalman filter for the FA strain generally performs less good than the other algorithms. It is also observed that, for parked conditions, including strain data in the Kalman filter does not improve the results for all data sets. This indicates the presence of modeling errors. The same holds for the two other algorithms.

The results shown in Figs. 9 – 20 and Tables 2 and 3 are obtained by including the first six bending modes of the turbine in the system model, and accounting for all available acceleration and strain data obtained at the three highest levels. All algorithms can also be used with a reduced number of sensors and/or modes, however. This might be particularly beneficial when some modes are not participating in the vibration, e.g. higher order modes in parked conditions, or when a sensor is hitting the noise floor. For the datasets used in this contribution, it is seen that such an optimization is possible, yielding promising results. The optimized settings need to be verified over a long period to assure their robustness against environmental and operational variability, however, and are therefore not shown in this paper. As such, the optimization of the proposed techniques based on a variation of the number of modes included and the sensors used is part of future work.

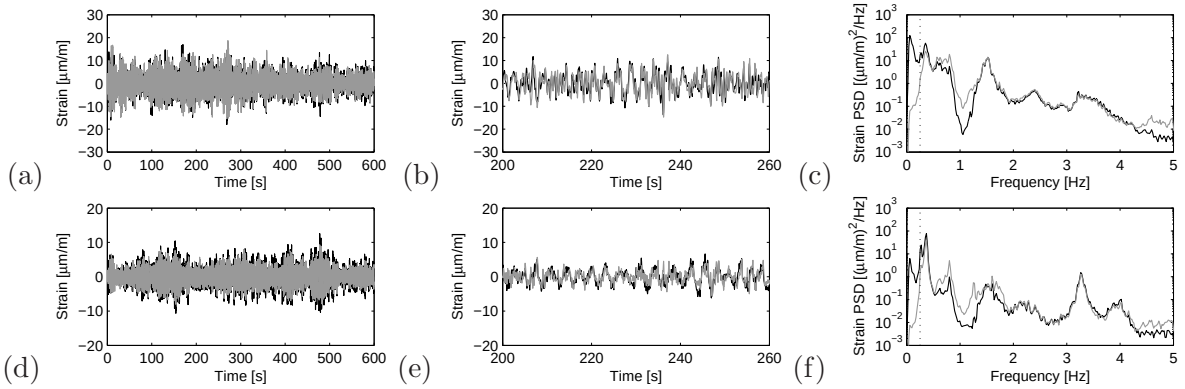

Fig. 9: Time history (left), detail time history (middle) and estimated PSD (right) of the FA strain (top) and SS strain (bottom) at level $h = 19$ m LAT for **data set 1** (rotating conditions), **sensor configuration $\boldsymbol{S_1}$**. The measured strains are shown in black, the estimated strains obtained from the **Kalman filter** are shown in gray.

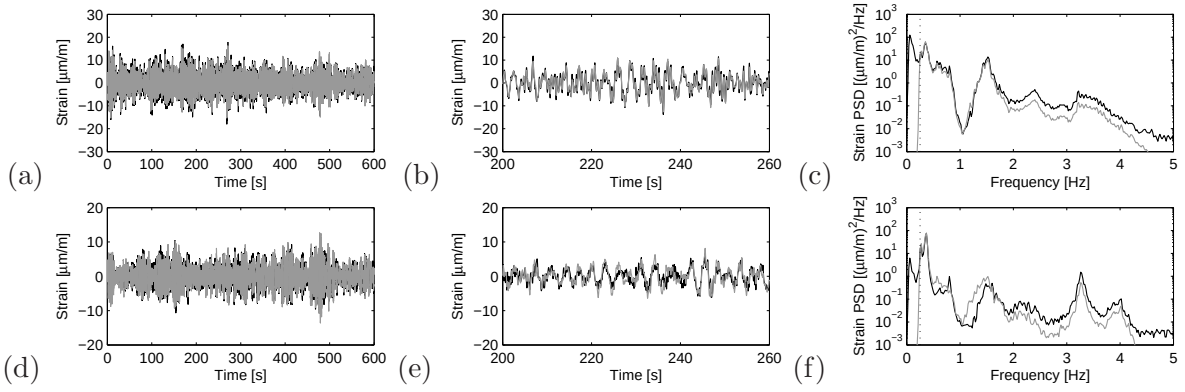

Fig. 10: Time history (left), detail time history (middle) and estimated PSD (right) of the FA strain (top) and SS strain (bottom) at level $h = 19$ m LAT for **data set 1** (rotating conditions), **sensor configuration $\boldsymbol{S_1}$**. The measured strains are shown in black, the estimated strains obtained from the **joint input-state estimation algorithm** are shown in gray.

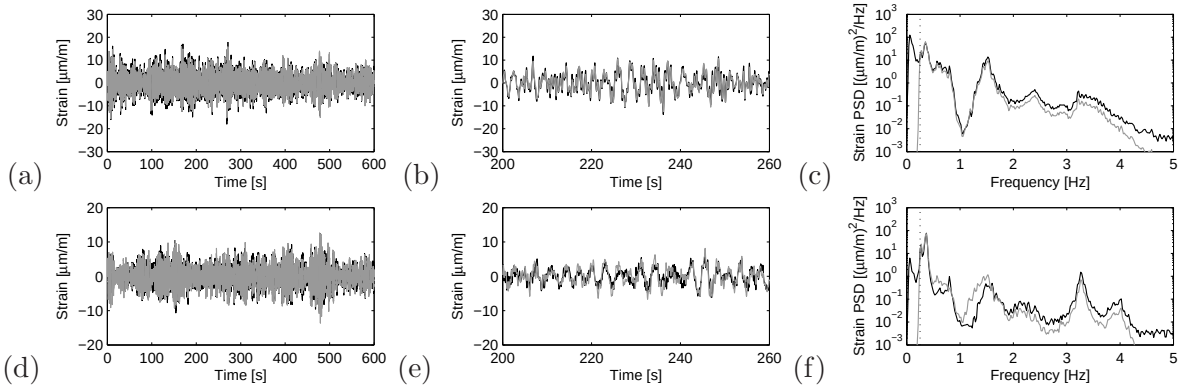

Fig. 11: Time history (left), detail time history (middle) and estimated PSD (right) of the FA strain (top) and SS strain (bottom) at level $h = 19$ m LAT for **data set 1** (rotating conditions), **sensor configuration $\boldsymbol{S_1}$**. The measured strains are shown in black, the estimated strains obtained from the **modal expansion algorithm** are shown in gray.

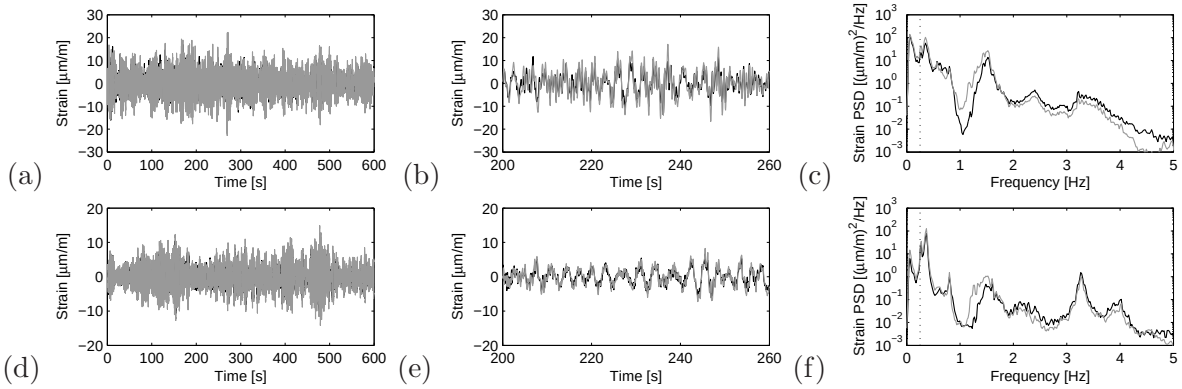

Fig. 12: Time history (left), detail time history (middle) and estimated PSD (right) of the FA strain (top) and SS strain (bottom) at level $h = 19$ m LAT for **data set 1** (rotating conditions), **sensor configuration S_2**. The measured strains are shown in black, the estimated strains obtained from the **Kalman filter** are shown in gray.

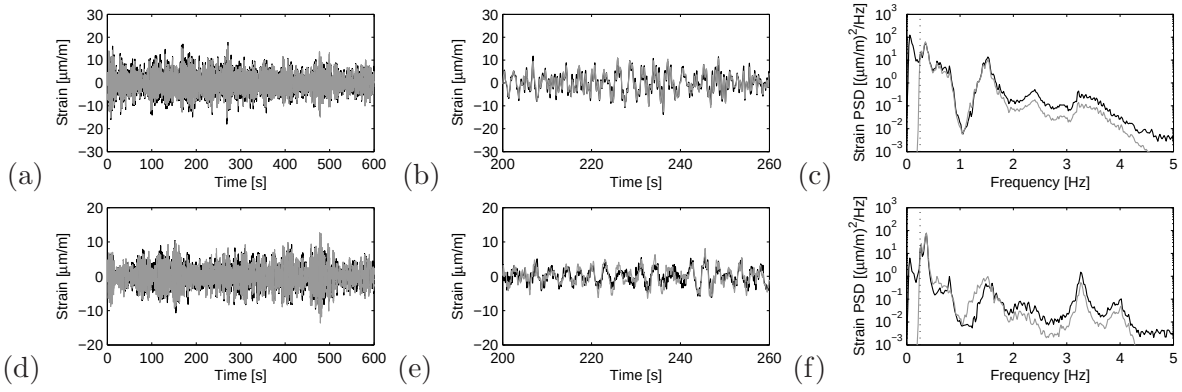

Fig. 13: Time history (left), detail time history (middle) and estimated PSD (right) of the FA strain (top) and SS strain (bottom) at level $h = 19$ m LAT for **data set 1** (rotating conditions), **sensor configuration S_2**. The measured strains are shown in black, the estimated strains obtained from the **joint input-state estimation algorithm** are shown in gray.

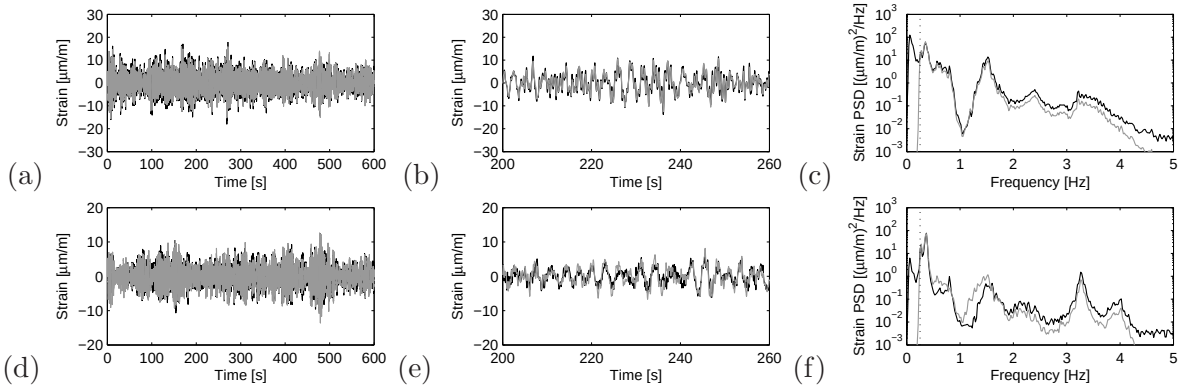

Fig. 14: Time history (left), detail time history (middle) and estimated PSD (right) of the FA strain (top) and SS strain (bottom) at level $h = 19$ m LAT for **data set 1** (rotating conditions), **sensor configuration S_2**. The measured strains are shown in black, the estimated strains obtained from the **modal expansion algorithm** are shown in gray.

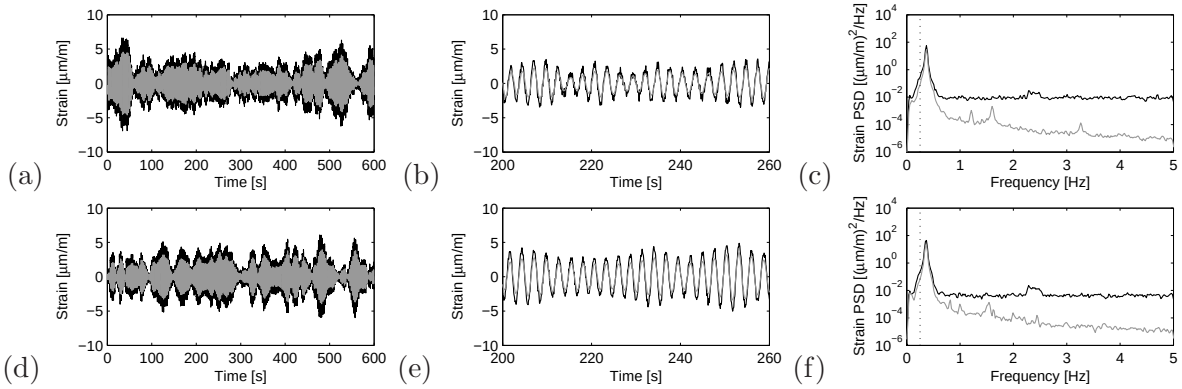

Fig. 15: Time history (left), detail time history (middle) and estimated PSD (right) of the FA strain (top) and SS strain (bottom) at level $h = 19$ m LAT for **data set 5** (parked conditions), **sensor configuration $\boldsymbol{S_1}$**. The measured strains are shown in black, the estimated strains obtained from the **Kalman filter** are shown in gray.

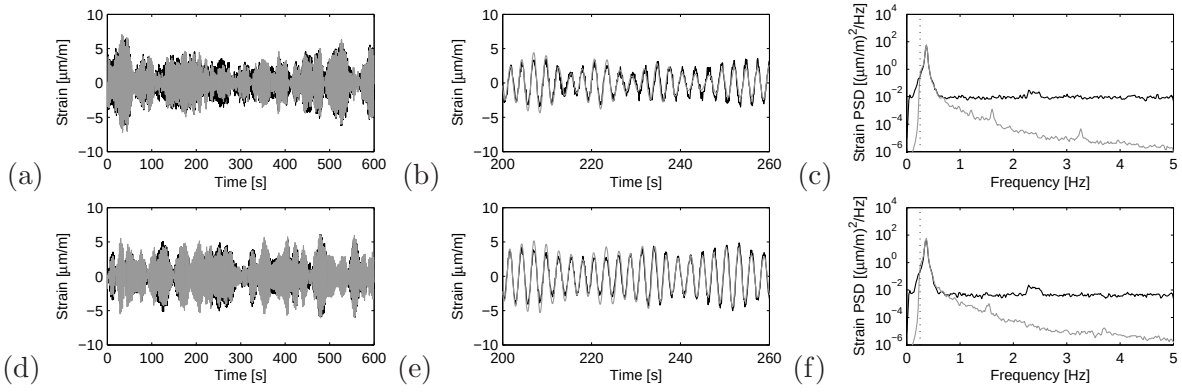

Fig. 16: Time history (left), detail time history (middle) and estimated PSD (right) of the FA strain (top) and SS strain (bottom) at level $h = 19$ m LAT for **data set 5** (parked conditions), **sensor configuration $\boldsymbol{S_1}$**. The measured strains are shown in black, the estimated strains obtained from the **joint input-state estimation algorithm** are shown in gray.

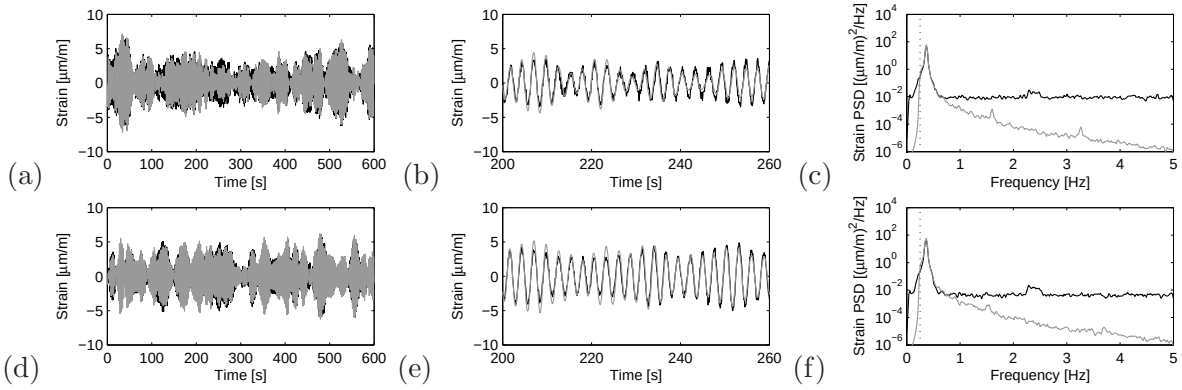

Fig. 17: Time history (left), detail time history (middle) and estimated PSD (right) of the FA strain (top) and SS strain (bottom) at level $h = 19$ m LAT for **data set 5** (parked conditions), **sensor configuration $\boldsymbol{S_1}$**. The measured strains are shown in black, the estimated strains obtained from the **modal expansion algorithm** are shown in gray.

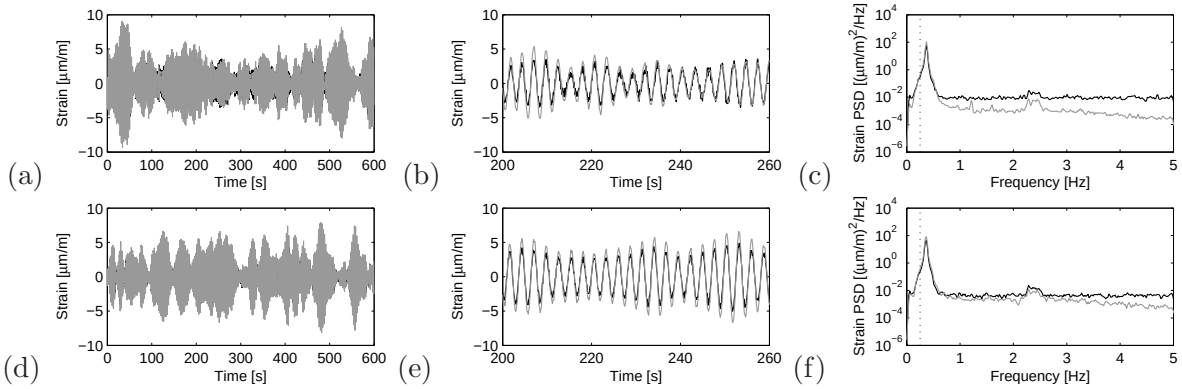

Fig. 18: Time history (left), detail time history (middle) and estimated PSD (right) of the FA strain (top) and SS strain (bottom) at level $h = 19$ m LAT for **data set 5** (parked conditions), **sensor configuration S_2**. The measured strains are shown in black, the estimated strains obtained from the **Kalman filter** are shown in gray.

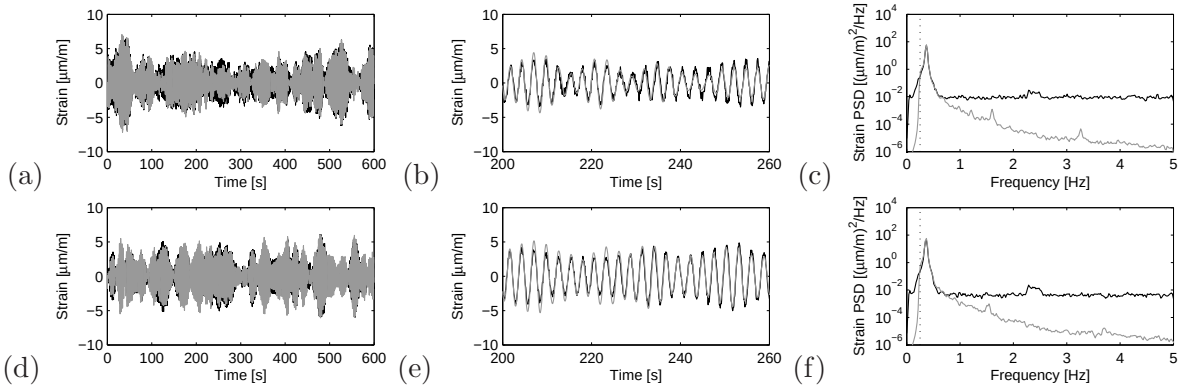

Fig. 19: Time history (left), detail time history (middle) and estimated PSD (right) of the FA strain (top) and SS strain (bottom) at level $h = 19$ m LAT for **data set 5** (parked conditions), **sensor configuration S_2**. The measured strains are shown in black, the estimated strains obtained from the **joint input-state estimation algorithm** are shown in gray.

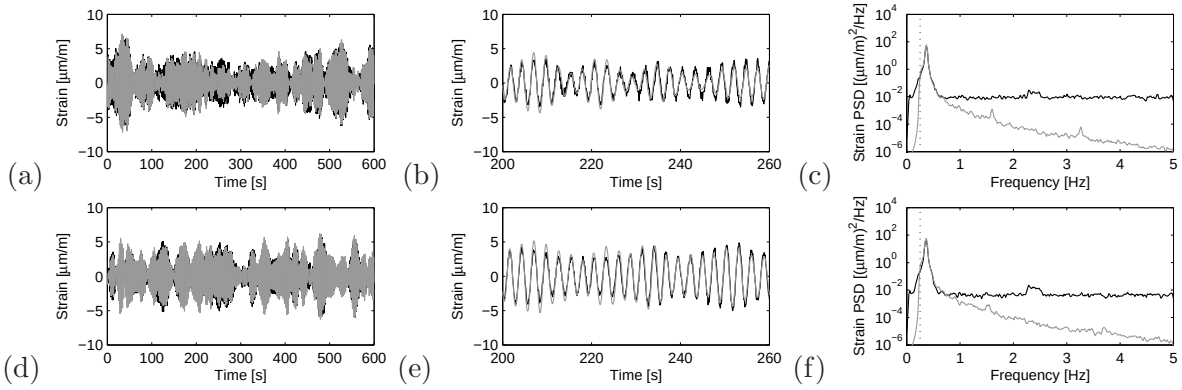

Fig. 20: Time history (left), detail time history (middle) and estimated PSD (right) of the FA strain (top) and SS strain (bottom) at level $h = 19$ m LAT for **data set 5** (parked conditions), **sensor configuration S_2**. The measured strains are shown in black, the estimated strains obtained from the **modal expansion algorithm** are shown in gray.

			TRAC [-]			MAE [μm/m]		
	data	config.	KF	JISE	ME	KF	JISE	ME
FA strain	set 1	S_1	0.59	0.94	0.94	2.34	0.87	0.89
		S_2	0.85	0.94	0.94	1.84	0.87	0.88
	set 2	S_1	0.68	0.92	0.92	1.45	0.72	0.73
		S_2	0.90	0.92	0.92	1.37	0.71	0.73
	set 3	S_1	0.66	0.93	0.93	1.47	0.68	0.68
		S_2	0.88	0.93	0.93	1.34	0.68	0.68
	set 4	S_1	0.61	0.94	0.94	2.12	0.79	0.79
		S_2	0.85	0.94	0.94	1.70	0.79	0.79
SS strain	set 1	S_1	0.75	0.80	0.79	1.29	1.19	1.23
		S_2	0.95	0.80	0.79	0.87	1.18	1.23
	set 2	S_1	0.85	0.90	0.90	1.29	0.92	0.94
		S_2	0.97	0.90	0.90	0.87	0.92	0.94
	set 3	S_1	0.83	0.88	0.87	1.27	0.94	0.97
		S_2	0.97	0.88	0.88	0.85	0.94	0.97
	set 4	S_1	0.78	0.82	0.80	1.27	1.14	1.18
		S_2	0.97	0.82	0.80	0.82	1.13	1.17

Table 2: Comparison of the TRAC and MAE values for **rotating conditions** (KF: Kalman filter, JISE: joint input-state estimation algorithm, ME: modal expansion algorithm).

			TRAC [-]			MAE [μm/m]		
	data	config.	KF	JISE	ME	KF	JISE	ME
FA strain	set 1	S_1	0.96	0.92	0.92	0.60	0.50	0.50
		S_2	0.95	0.92	0.92	0.73	0.49	0.50
	set 2	S_1	0.96	0.91	0.91	0.57	0.47	0.48
		S_2	0.95	0.91	0.91	0.61	0.47	0.47
	set 3	S_1	0.97	0.94	0.94	0.65	0.47	0.47
		S_2	0.96	0.94	0.94	0.74	0.47	0.47
	set 4	S_1	0.96	0.92	0.92	0.60	0.49	0.49
		S_2	0.96	0.92	0.92	0.64	0.49	0.49
SS strain	set 1	S_1	0.96	0.88	0.88	0.58	0.64	0.65
		S_2	0.98	0.88	0.88	0.62	0.63	0.65
	set 2	S_1	0.96	0.83	0.82	0.47	0.60	0.61
		S_2	0.98	0.83	0.82	0.53	0.60	0.61
	set 3	S_1	0.96	0.82	0.82	0.53	0.68	0.69
		S_2	0.98	0.82	0.82	0.54	0.68	0.69
	set 4	S_1	0.95	0.81	0.81	0.50	0.62	0.63
		S_2	0.98	0.81	0.81	0.53	0.62	0.63

Table 3: Comparison of the TRAC and MAE values for **parked conditions** (KF: Kalman filter, JISE: joint input-state estimation algorithm, ME: modal expansion algorithm).

3.5. Low frequency strains

As discussed in the introduction, the current paper focuses on dynamic strain estimation. There are two problems when the proposed methods are applied to predict the low frequency strains, induced by the thrust-loading. The first concern is the conversion from accelerations to strains. The integration inevitably requires a double integration, which risks to blow up the low frequency noise in the measured accelerations, resulting in large errors in the low frequency components of the predicted strains. This is illustrated in Fig. 21, which compares the PSD of the (unfiltered) strain ϵ_{19FA}, obtained from the modal expansion algorithm, to the measured strains (data set 5, parked conditions, sensor configuration S_1). The figure also shows how at low frequencies (< 0.25 Hz) and higher frequencies (> 0.7 Hz) the PSD of the estimated strain signal follows the $1/\omega^4$ behavior that originates from the measurement noise on the acceleration data, as already mentioned in Section 3.4. The figure reveals that the near-static strains below 0.25 Hz obtained from the estimation are predominantly due to measurement noise, which have therefore been removed in this paper by filtering. Note that the use of accelerometers with better noise properties can push this lower frequency bound further down.

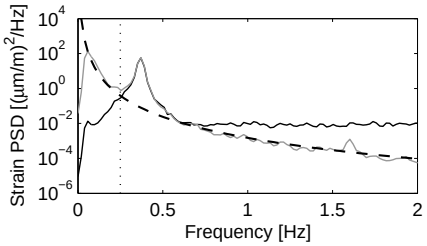

Fig. 21: PSD of the measured (black) and estimated (gray) FA strain at level $h = 19$ m LAT for data set 5 (parked conditions), sensor configuration S_1. The estimated strain is obtained from the modal expansion algorithm. The black dashed line shows a $1/\omega^4$ curve fit, in order to illustrate the influence of noise on the acceleration data.

The second potential problem is more fundamental to the concept. All techniques applied in this paper rely upon modal decomposition. A small number of modes, that contribute to the dynamic response in the frequency range from 0.25 to 5 Hz, is included. At low frequencies, a much larger number of modes is required to describe the near-static behavior of the turbine. The resulting extrapolation can yield erroneous results, as the static deflection patterns of the turbine might not be accurately described by a small number of dynamic modes.

In this contribution, the lower frequency bound was set to 0.25 Hz to avoid both problems, yet try to capture as many dynamics as possible, including wave induced vibrations. For the Belgian coast, wave periods exceeding 5 s are fairly common (wave frequency $\leq$0.2 Hz), however, implying that the current methods might need further improvement or sensors with better noise properties.

4. Future work

The main focus for future work is to combine the estimated dynamic strains with estimates of the near-static strains in order to predict the entire strain time history. The resulting method will need to be validated over the entire range of operational and environmental conditions the turbine is subjected to, for example to assess the ability to capture the low frequent wave loading. As fatigue life estimation is the main driver of this research, the results have to be evaluated on their ability to correctly estimate the fatigue spectra over a long period of time.

The dynamic strain prediction algorithms themselves can still be further developed, with a particular interest for frequency dependent weighing. This will allow the algorithms to optimally use the best performing sensors in each frequency band.

5. Conclusions

In this paper, three algorithms for response estimation in structural dynamics have been considered: a Kalman filter algorithm, a joint input-state estimation algorithm, and a modal expansion algorithm. The algorithms have been applied to data obtained from a monitoring campaign on an offshore Vestas V90 3 MW wind turbine on a monopile foundation, hereby estimating the strains in the tower of the wind turbine based on a set on response measurements and a system model. Both parked and rotating conditions are considered. The paper focuses on dynamic strain estimation and therefore does not consider low frequency strains induced by thrust-loading. All algorithms are evaluated using acceleration data only, as well as a combination of acceleration and strain data. For rotating conditions, both the joint input-state estimation algorithm and the modal expansion algorithm yield satisfactory results with only minor improvement by inclusion of measured strains. Including measured strains significantly improves the results of the Kalman filter, however, which for sideways motion become superior to the results obtained from the two other techniques. For parked conditions, the three techniques again yield satisfactory results, with the Kalman filter performing well without strain data.
In general, it can be concluded that the three techniques for this application are competitive and interchangeable. Most importantly, the three techniques have proven that in the near future accelerometers can replace and potentially outperform regular strain sensors to assess the dynamic strain contributions in offshore wind turbine foundations.

Acknowledgments

The research presented in this paper has been performed within the framework of the project G.0738.11 Inverse identification of wind loads on structures, funded by the Research Foundation Flanders (FWO), Belgium. The financial support of FWO is gratefully acknowledged. The authors affiliated to KU Leuven are all members of the KU Leuven - BOF PFV/10/002 OPTEC - Optimization in Engineering Center. The authors would also like to acknowledge the Offshore Wind Infrastructure Application Lab, Parkwind and Belwind for providing the data that has been used throughout this paper.

References

[1] R. Baudisch, Structural Health Monitoring of Offshore Wind Turbines, Master's thesis, Danmarks Tekniske Universitet, 2012.
[2] P. Guillaume, E. Parloo, G. De Sitter, Source identification from noisy response measurements using an iterative weighted pseudo-inverse approach., in: Proceedings of ISMA2002 International Conference on Noise and Vibration Engineering, Leuven, Belgium, pp. 1817–1824.
[3] M. Klinkov, C. Fritzen, An updated comparison of the force reconstruction methods, Key Engineering Materials 347 (2007) 461–466.
[4] E. Jacquelin, A. Bennani, P. Hamelin, Force reconstruction: analysis and regularization of a deconvolution problem, Journal of Sound and Vibration 265 (2003) 81–107.
[5] Z. Lu, S. Law, Force identification based on sensitivity in time domain, ASCE Journal of Engineering Mechanics 132 (2006) 1050–1056.

[6] S. Law, J. Bu, X. Zhu, Time-varying wind load identification from structural responses, Engineering Structures 27 (2005) 1586–1598.
[7] J. Liu, C. Ma, I. Kung, D. Lin, Input force estimation of a cantilever plate by using a system identification technique, Computer Methods in Applied Mechanics and Engineering 190 (2000) 1309–1322.
[8] C. Ma, J. Chang, D. Lin, Input forces estimation of beam structures by an inverse method, Journal of Sound and Vibration 259 (2003) 387–407.
[9] C. Ma, C. Ho, An inverse method for the estimation of input forces acting on non-linear structural systems, Journal of Sound and Vibration 275 (2004) 953–971.
[10] S. Xu, X. Deng, V. Tiwari, M. Sutton, W. Fourney, D. Bretall, An inverse approach for pressure load identification, International Journal of Impact Engineering 37 (2010) 865 – 877.
[11] S. Eftekhar Azam, C. Papadimitriou, E. Chatzi, A dual Kalman filter approach for state estimation via output-only acceleration measurements, Mechanical Systems and Signal Processing 60–61 (2015) 866–886.
[12] J. Hwang, A. Kareem, W. Kim, Estimation of modal loads using structural response, Journal of Sound and Vibration 326 (2009) 522–539.
[13] J. Hwang, A. Kareem, H. Kim, Wind load identification using wind tunnel test data by inverse analysis, Journal of Wind Engineering and Industrial Aerodynamics 326 (2011) 18–26.
[14] Y. Niu, C.-P. Fritzen, I. Buethe, Online simultaneous reconstruction of wind load and structural responses - theory and application to canton tower, Computer-Aided Civil and Infrastructure Engineering 30 (2015) 666–681.
[15] M. Klinkov, C. Fritzen, Wind load observer for a 5 mw wind energy plant, in: Proceedings of IMAC XXVIII International Modal Analysis Conference, Jacksonville, Florida USA.
[16] H. Hjelm, R. Brincker, J. Graugaard-Jensen, K. Munch, Determination of stress histories in structures by natural input modal analysis, in: Proceedings of IMAC XXIII International Modal Analysis Conference, Houston, Texas, pp. 838–844.
[17] P. Avitabile, P. Pingle, Prediction of full field dynamic strain from limited sets of measured data, Shock and Vibration 19 (2012) 765–785.
[18] M. López Aenlle, L. Hermanns, P. Fernández, A. Fraile, Stress estimation in a scale model of a symetric two story building, in: A. Cunha, L. Ramos, E. Caetano, P. Lourenço (Eds.), Proceedings of the 5th International Operational Modal Analysis Conference, IOMAC 2013, Guimarães, Portugal.
[19] A. Iliopoulos, R. Shirzadeh, W. Weijtjens, P. Guillaume, D. Van Hemelrijck, C. Devriendt, A modal decomposition and expansion approach for prediction of dynamic responses on a monopile offshore wind turbine using a limited number of vibration sensors, Mechanical Systems and Signal Processing 68–69 (2016) 84–104.
[20] E. Yazid, S. Mohd, P. Setyamartan, Time-varying spectrum estimation of offshore structure response based on a time-varying autoregressive model, Journal of Applied Sciences 12 (2012) 2383–2389.
[21] C. Papadimitriou, C.-P. Fritzen, P. Kraemer, E. Ntotsios, Fatigue predictions in entire body of metallic structures from a limited number of vibration sensors using Kalman filtering, Structural Control and Health Monitoring 18 (2011) 554–573. Published online in Wiley InterScience (www.interscience.wiley.com). DOI:10.1002/stc.395.
[22] A. Smyth, M. Wu, Multi-rate Kalman filtering for the data fusion of displacement and acceleration response measurements in dynamic system monitoring, Mechanical Systems and Signal Processing 21 (2007) 706–723.
[23] R. Palanisamy, S. Cho, H. Kim, S.-H. Sim, Experimental validation of Kalman filter-based strain estimation in structures subjected to non-zero mean input, Smart Structures and Systems 15 (2015) 489–503.
[24] H. Jo, B. Spencer, Multi-Metric model-based structural health monitoring, in: J. P. Lynch, K.-W. Wang, H. Sohn (Eds.), Proceedings of SPIE 9061, Sensors and Smart Structures Technologies for Civil, Mechanical, and Aerospace Systems 2014, San Diego, California, USA.
[25] E. Chatzi, A. Smyth, The unscented Kalman filter and particle filter methods for nonlinear structural system identification with non-collocated heterogeneous sensing, Structural Control and Health Monitoring 16 (2009) 99–123.
[26] M. Wu, A. Smyth, Application of the unscented Kalman filter for real-time nonlinear structural system identification, Structural Control and Health Monitoring 14 (2007) 971–990.
[27] S. Mariani, A. Corigliano, Impact induced composite delamination: state and parameter identification via joint and dual extended kalman filters, Computer Methods in Applied Mechanics and Engineering 194 (2005) 5242–5272.
[28] J. Ching, J. Beck, K. Porter, Bayesian state and parameter estimation of uncertain dynamical systems, Probabilistic Engineering Mechanics 21 (2006) 81–96.
[29] E. Chatzi, A. Smyth, Nonlinear system identification: Particle-based methods, in: M. Beer, I. Kougioumtzoglou,

E. Patelli, I.-K. Au (Eds.), Encyclopedia of Earthquake Engineering, Springer, London, UK, 2014.
[30] C. Devriendt, F. Magalhães, W. Weijtjens, G. De Sitter, A. Cunha, P. Guillaume, Structural health monitoring of offshore wind turbines using automated operational modal analysis, in: F.-K. Chang (Ed.), Proceedings of the 9th International Workshop on Structural Health Monitoring, IWSHM 2013, volume 1, Stanford, CA, USA, pp. 2415–2422.
[31] S. Gillijns, B. De Moor, Unbiased minimum-variance input and state estimation for linear discrete-time systems with direct feedthrough, Automatica 43 (2007) 934–937.
[32] E. Lourens, C. Papadimitriou, S. Gillijns, E. Reynders, G. De Roeck, G. Lombaert, Joint input-response estimation for structural systems based on reduced-order models and vibration data from a limited number of sensors, Mechanical Systems and Signal Processing 29 (2012) 310–327.
[33] P. Van der Male, E. Lourens, Operational vibration-based response estimation for offshore wind lattice structures, in: Structural Health Monitoring and Damage Detection, Volume 7: Proceedings of the 33rd IMAC, A Conference and Exposition on Structural Dynamics, 2015, Springer, p. 83.
[34] K. Maes, A. Smyth, G. De Roeck, G. Lombaert, Joint input-state estimation in structural dynamics, Mechanical Systems and Signal Processing 70–71 (2016) 445–466.
[35] A. Chopra, Dynamics of structures. Theory and applications to earthquake engineering, Pearson Prentice-Hall, Upper Saddle River, NJ, fourth edition, 2012.
[36] P. Van Overschee, B. De Moor, Subspace algorithm for the stochastic identification problem, Automatica 29 (1993) 649–660.
[37] E. Reynders, G. De Roeck, Reference-based combined deterministic-stochastic subspace identification for experimental and operational modal analysis, Mechanical Systems and Signal Processing 22 (2008) 617–637.
[38] R. E. Kalman, On the general theory of control systems, in: Proceedings of the First International Congress of IFAC, Moscow.
[39] Y. Niu, M. Klinkov, C.-P. Fritzen, Online force reconstruction using an unknown-input Kalman filter approach., in: Proceedings of the 8th International Conference on Structural Dynamics, EURODYN 2011, Leuven, Belgium, pp. 2569–2576.
[40] K. Maes, E. Lourens, K. Van Nimmen, E. Reynders, G. De Roeck, G. Lombaert, Design of sensor networks for instantaneous inversion of modally reduced order models in structural dynamics, Mechanical Systems and Signal Processing 52–53 (2015) 628–644.
[41] W. Weijtjens, Advanced methods for estimating and monitoring the modal parameters of operational systems subjected to non-white excitation, Ph.D. thesis, Vrije Universiteit Brussel, 2014.
[42] M. Häckell, R. Rolfes, Monitoring a 5mw offshore wind energy converter - condition parameters and triangulation based extraction of modal parameters, Mechanical Systems and Signal Processing 40 (2013) 322–343.
[43] K. Maes, G. De Roeck, G. Lombaert, Response estimation in structural dynamics, in: A. Cunha, E. Caetano, P. Ribeiro, G. Müller (Eds.), Proceedings of the 9th International Conference On Structural Dynamics, EURODYN 2014, Porto, Portugal, pp. 2399–2406.
[44] C. Devriendt, W. Weijtjens, M. El Kafafy, G. De Sitter, Monitoring resonant frequencies and damping values of an offshore wind turbine in parked conditions, IET Renewable Power Generation 8 (2014) 433 – 441. Doi: 10.1049/iet-rpg.2013.0229.
[45] R. Allemang, D. Brown, A correlation coefficient for modal vector analysis, in: Proceedings of the 1st International Modal Analysis Conference, Orlando, FL, pp. 110–116.
[46] W. Weijtjens, T. Verbelen, G. De Sitter, C. Devriendt, Foundation structural health monitoring of an offshore wind turbinea full-scale case study, Structural Health Monitoring (2015). In press.
[47] K. Maes, K. Van Nimmen, E. Lourens, A. Rezayat, P. Guillaume, G. De Roeck, G. Lombaert, Verification of joint input-state estimation for force identification by means of in situ measurements on a footbridge, Mechanical Systems and Signal Processing (2016). Accepted for publication.